受入
93-12-137
高工研図書室

EUROPEAN ORGANIZATION FOR NUCLEAR RESEARCH

CERN-PPE/93-154
5 August 1993

The Forward Ring Imaging Cherenkov detector of DELPHI

W. Adam[1], E. Albrecht[1], I. Ambec[12], A. Augustinus[10], C. Barnoux[5], B. Boštjančič[1,8], O. Botner[12], A.P. Budziak[7], L.P. Caloba[2], P. Carecchio[5], P. Cavalli[5], L. Ceelie[10], R. Cereseto[4], G. Cerutti[1], E. Dahl-Jensen[9], Ph. Dam[9], G. Damgaard[9], N. de Koning[10], A.S. de la Vega[2], N. Dimitriou[3], W. Dulinski[7a], L-O. Eek[12], T. Ekelöf[12], J. Erikson[12], A. Florek[7], B. Florek[7], F. Fontanelli[4], A. Fontenille[5], K. Galuszka[7], J. Garcia[11], V. Gracco[4], A. Hallgren[12], W. Hao[10], T. Henkes[1], D. Isenhower[1b], H. Johansson[12], E. Karvelas[3], P. Kindblom[12], B. Koene[10], A. Korporaal[10], P. Kostarakis[3], G. Lenzen[13], L-E. Lindqvist[12], P. Lorenz[13c], D. Loukas[3], B.Lund-Jensen[12d], A. Maltezos[3], A. Markou[3], L. Mattsson[12], J. Medbo[12], J. Michalowski[7], F. Montano[4], B.S. Nielsen[9], J.M. Ostler[1], K. Pakonski[7], C. Perdikis[3], G. Polok[7], A. Robohm[6], G. Sajot[5], M. Sannino[4], E. Saragas[3], E. Schyns[13], S. Squarcia[4], G. Stavropoulos[3], M. Stodulski[7], Z. Stopa[7], J. Thadome[13], G.E. Theodosiou[3], L. Traspedini[4], M. Turala[7], O. Ullaland[1], A. Wärm[12], J. Werner[13], S. Xyroutsikos[3], M. Zavrtanik[8] and E. Zevgolatakos[3]

Abstract

The Forward Ring Imaging Cherenkov detector of the DELPHI experiment at LEP provides hadron identification at polar angles $15° < \theta < 35°$ and $145° < \theta < 165°$. Two radiator media, a layer of liquid C_6F_{14} and a volume of gaseous C_4F_{10}, in combination provide coverage of momenta up to 40 GeV/c. A single array of photosensitive Time Projection Chambers registers the impact points of ultraviolet photons from both radiators. The design of the detector and of its readout system is described. First results obtained with a partly installed detector are reported.

(Submitted to Nucl. Instr. and Meth.)

[1] CERN, CH-1211 Geneva 23, Switzerland
[2] COPPE/UFRJ, Dept. de Fisicà, Universidad Federal do Rio de Janeiro, Ilha do Fundão, 21945 Rio de Janeiro, Brazil
[3] Institute of Nuclear Physics, N.C.S.R. 'Demokritos', P.O. Box 60228, GR-15310 Aghia Paraskevi, Attiki, Greece
[4] Dipartimento di Fisica, Università di Genova and INFN, Via Dodecaneso 33, I-16146 Genova, Italy
[5] Institut des Sciences Nucléaires, Université de Grenoble 1, F-38026 Grenoble, France
[6] Institut für Experimentelle Kernphysik, Universität Karlsruhe, Postfach 6980, D-7500 Karlsruhe 1, Germany
[7] High Energy Physics Laboratory, Inst. of Nucl. Physics, Ul. Kawiory 26a, PL-30055 Krakow 30, Poland
[8] Institut 'Jozef Stefan', Ljubljana, Slovenija
[9] Niels Bohr Institute, Blegdamsvej 17, DK-2100 Copenhagen, Denmark
[10] NIKHEF-H, Postbus 41882, NL-1009 DB Amsterdam, The Netherlands
[11] Facultad de Ciencias, Universidad de Santander, av. de los Castros, E-39005 Santander, Spain
[12] Dept. of Radiation Sciences, University of Uppsala, P.O. Box 535, S-751 21 Uppsala, Sweden
[13] Fachbereich Physik, University of Wuppertal, Postfach 100 127, D-5600 Wuppertal 1, Germany
[a] Present address: IN2P3-CNRS/ULP, Strasbourg, France
[b] Visitor from Abilene Christian Univ., Texas, USA
[c] Present address: Bayer Leverkusen, Germany
[d] Present address: MSI, Stockholm, Sweden

1 Introduction

The DELPHI experiment [1] at the Large Electron Positron collider (LEP) at CERN is equipped with Ring Imaging Cherenkov (RICH) detectors for the identification of pions, kaons and protons over most of the momentum range below 40 GeV/c. The RICH system covers almost the full solid angle. It consists of two end-cap detectors, together referred to as the Forward RICH, and a detector of cylindrical geometry in the central region, the Barrel RICH. Fig.1 shows their positions within the DELPHI assembly. The Forward RICH detectors cover the polar angles $15° < \theta < 35°$ and $145° < \theta < 165°$. Although very different in geometry, the Barrel and Forward RICH employ the same principles. Cherenkov photons in the UV range from both liquid and gaseous radiators are detected in a single array of photosensitive Time Projection Chambers (TPC). From the photon coordinates measured in the TPC plane, emission angles with respect to particle tracks are reconstructed. For a given particle momentum, mass hypotheses are tested against the observed number of photons and the distribution of Cherenkov angles of individual photons. The RICH counters are not stand-alone instruments. They rely on tracking detectors, not only for the determination of particle momenta, but also for the elimination of systematic errors in track coordinates. Track segments measured in the RICH itself are shifted towards too small drift times, since the single-electron sensitivity leads to registration of the leading edge of the dE/dx signal. The Forward RICH is sandwiched between two tracking chambers (numbers 11 and 14 in fig. 1). Furthermore, the track detectors in the central region of DELPHI contribute to forward tracking down to $\theta = 20°$.

The development of the DELPHI RICH detectors was initiated by the work reported in [2]. Subsequent development work within the DELPHI collaboration has been documented in [3] and references therein. The Forward RICH detectors have been fully installed before the 1993 LEP run. This paper describes the detector construction and first results obtained with one of the four 180° segments, which has already been operated throughout the 1992 run.

Fig.2 shows the arrangement of the principal parts of the Forward RICH. One detector consists of two 180° segments, joined together in the vertical plane. These in turn are assembled out of two parts: a main vessel that houses the photon detector and mirrors and serves as gas radiator volume, and a shallower vessel, flanged onto the main vessel, which carries the liquid radiator containers. The assembly extends 940 mm along the LEP beampipe, starting at ± 1720 mm from the interaction point. The radial extension runs from 450 mm to 1250 (1800) mm at the front (back) face. Inside the vessels, components are arranged in sectors spanning 30° in azimuth. A sector contains three thin liquid radiator containers, a photon detector and a set of five spherical mirrors. The gas radiator fills the space between these objects. Whilst light from the approximately 60 cm deep gas radiator is focussed onto the detection plane by the mirrors, photons from the 1 cm deep liquid radiator layer are directly incident on the photon detector. The resulting error on the reconstructed Cherenkov angle due to the uncertainty on the photon emission depth is small compared to the effect of finite position resolution in the detection plane. The photon detector consists of a segmented TPC with UV-grade quartz windows. The drift-gas contains an admixture of the photo-ionizing vapour Tetrakis-diMethylAmino-Ethylene (TMAE) [4]. Photoelectrons drift azimuthally towards Multi Wire Proportional Chambers (MWPC), mounted along the long sides of the trapezoidal drift volume. The chambers are equipped with anode and cathode-strip readout, providing a 3-D reconstruction of photoconversion points. At TMAE concentrations corresponding to its saturated vapour pressure at 25 °C, the photon mean free path is about 2 cm. Since photons from the

liquid and gas radiators enter the 6 cm deep drift volume from opposite sides, the depth coordinate of photoelectrons tags their origin. The most consequential difference between the Forward and Barrel RICH detectors is the fact that in the Forward RICH photoelectron drift occurs in a plane perpendicular to the 1.2 Tesla magnetic field of DELPHI. The resulting Lorentz angle between drift trajectories and the electric field has important consequences for the MWPC design and for the choice of driftgas.

The TMAE ionization potential, 5.4 eV, sets the lower bound on the photon energy window. The upper bound, 7.1 eV and 7.5 eV for photons from the liquid and gas radiators respectively, is set by the radiator and quartz transmittance cutoffs. Expressed in wavelengths, the acceptance windows are approximately 175 – 230 nm (liquid) and 165 – 230 nm (gas). Chromatic dispersion, i.e. variation of the refractive index of the radiator substances over this energy window, sets a limit *ab initio* on the Cherenkov angle resolution. Perfluorocarbons were chosen as radiator media because of their low chromatic dispersion, combined with a transmission cutoff that almost matches that of the quartz windows employed. The liquid radiators consist of 1 cm thick layers of perfluorohexane (C_6F_{14}) in front of quartz exit windows. The gas radiator volume is filled with perfluorobutane (C_4F_{10}). Properties of these substances are given in table 1. The three fluid systems (gas radiator, liquid radiator and driftgas) are referenced to atmospheric pressure.

Table 1: The physical properties of C_4F_{10}, C_5F_{12} and C_6F_{14}.

	C_4F_{10}	C_5F_{12}	C_6F_{14}
Molecular weight (g/mol)	238	288	338
Boiling point (°C)	-1.7	28	57
Liquid density (g/cm^3) at b.p.	1.594	1.630	1.682
Gas density (g/cm^3)	$0.01195_{1.08bar}$	$0.0125_{1.0bar}$	
Vapour pressure (mbar) at -20 °C	450	57	
Refractive index at 7 eV	1.00153	1.00172	1.2827
Gas transparency (15 cm layer at 1 atm) 162 nm	1	0	
165 nm	1	0.58	
170 nm	1	0.80	

Initially, the heavier gas C_5F_{12} had been considered as gas radiator, since its larger index of refraction compared to C_4F_{10} would lead to a slightly better matching of the momentum ranges covered by the liquid and gas radiators. It also has a somewhat smaller chromatic dispersion. However, these advantages largely cancel against the fact that our measurements of UV transparencies show significantly better results for C_4F_{10} than for C_5F_{12}. Use of C_5F_{12} as gas radiator requires heating of the detector assembly to 35-40 °C. Although provisions for heating have been made, it was concluded that the marginal gain, if any, from a C_5F_{12} radiator does not warrant the complications of detector operation at elevated temperature.

2 Detector and support systems

2.1 Vessel

One Forward RICH detector is housed in two vessels of 180° in azimuth, each closed by a lid structure carrying the liquid radiator containers. The vessels are mounted on a

support tube (900 mm diameter, 1600 mm long) that is bolted into the iron of the endcap section of the magnet yoke. The tube is a 5 mm thick sandwich structure of carbon tissue and foam plate. Two reinforcement ribs of carbon-composite material (5 mm thick and 200 mm wide) run lengthwise along the top and bottom of the tube. Two carbon flange rings for vessel mounting are located at the free end and midway along the tube. The tube was tested under a load of 1000 kg (which is about the weight of a fully equipped detector) applied to the flange at the tube end. The measured deflection of the tube end was 2 mm.

The vessels are made of composite materials. The walls - 13 discrete sections per vessel - consist of two layers of 350 μm aramide tissue at the inner surface, separated by 18 mm of foam material[1] from 2 layers of 350 μm carbon tissue at the outer surface. Special moulds were made to laminate each multilayer wall section in one gluing operation. It was required that it should be possible to maintain the radiator gas at 40 °C, while keeping the outer surface of the vessel at 20 °C. Aramide tissue was chosen as inner sandwich layer because its thermal expansion coefficient is close to zero. Carbon tissue is used for the outer layer because of its high modulus of elasticity and good thermal conductivity (PVC water cooling pipes are embedded between the two carbon tissue layers). The foam layer serves as spacer and thermal insulator. The inner surface is covered with 80 μm thick kapton foil and an epoxy resin film between kapton sheets. The kapton foils carry printed heating strips. The back plane of the vessel contains fibre glass rings (five per 30° sector) for mirror mounting. Also incorporated in the vessel structure are frames for TPC mounting (a cast of epoxy resin mixed with cut fibre glass) and 20/18 mm tubes of carbon fibre that serve as reinforcement spokes in the TPC region. All elements were joined together by gluing[2]. Voltage degraders consisting of metallized kapton layers have been installed to assist in electrical field shaping. The gas radiator inlet and outlet are at the bottom and top of the vessel, respectively. Tests for leak tightness showed a 2 ppm level of oxygen contamination after 24 volume changes.

2.2 Liquid radiator

2.2.1 Mechanics

The liquid-radiator plane consists of 36 discrete containers of 1.0 cm depth filled with the fluorinated alkane C_6F_{14}[3]. The number of photons per particle obviously increases with the radiator thickness, but so does the uncertainty on their emission points. The combined effect is that the error on the Cherenkov angle is minimized when the radiator thickness is around 1 cm. The containers are mounted inside two semi-circular vessels that are flanged onto the main vessel structure (see fig. 2). The containers of a 180° segment are arranged as three concentric annuli of 6 containers each. A 30° azimuthal section is thus covered by a triplet of containers. A cut along the symmetry axis of a triplet produces the side view shown in fig. 3. The acceptance in polar angle is 16.3° - 34.6° . The containers are tilted with respect to the vertical mounting plane by 18.1° (inner), 21.7° (middle) and 28.6° (outer). These values result from a compromise between 1) the design criterion of placing the radiator surfaces approximately perpendicular to the average direction of incident particles, and 2) the need to retain a sufficient lever arm between the liquid radiator and the photon detection plane.

For particles that traverse a container near its large-radius edge, about half of the

[1] Rohacel, product of Röhm, Darmstadt.
[2] Araldite AW 106 mixed with silica powder.
[3] Suppliers: ISC, Bristol, UK (product code PP1) and 3M, Antwerp, Belgium (product code FC72)

Cherenkov photons are intercepted by the tray in the next annulus or by the vessel wall. In spite of this, the present geometry leads to a gain in resolution on the Cherenkov angle compared to the simpler solution of a flat radiator plane. In the latter case, the resolution deteriorates with increasing particle polar angle, both by loss of photons due to total reflection at the radiator exit window and by an increased average error per transmitted photon. Further, since the adopted geometry minimizes refraction of the Cherenkov light, the Cherenkov image on the detection plane occupies the smallest possible fiducial area, which optimizes the signal to background ratio.

The exit windows of the containers consist of UV-grade fused silica plates[4] of 5.0 mm thickness. All other parts of the liquid-radiator structure are constructed out of carbonfibre-epoxy composite material. A container essentially consists of a shallow tray inside a deeper one, with their rims at the same level. This produces a strong double-bottomed structure. The quartz window is glued[5] onto the top of the tray rims. Finally, in order to obtain a clamped quartz mounting, carbonfibre strips that grip over the quartz edges are glued along the sides of the trays. The containers are mounted on triangular supports, which have a gas-tight screw mounting onto the vessel. The mounting plane is a double- walled structure: two carbon-epoxy plates, each 2 mm thick, are separated by 6 mm of foam material[6]. An assembly jig assures correct positioning of the containers, referenced to the flange surface of the vessel. Kapton foils with a pattern of copper strips have been glued onto the inside walls of the vessel to allow heating. A water- cooled heat shield is attached to the outside.

2.2.2 Liquid circulation system

Liquid input and output ports are on diametrically opposite corners of a container, the output always being at the highest location. Each container is served by its own input capillary tube (1.5 mm inner diameter). The return line consists of a common sewer (14 mm inner diameter). The flow diagram of the C_6F_{14} circuit is shown in fig. 4. Cleaned liquid is pushed with an overpressure of approximately 2 bar from the distribution manifolds to the liquid containers via the 30 m long capillary tubes. Pressure sensors are installed on all input lines, 1-4 m away from the radiators. The control system (section 2.5) switches off any line where the differential pressure exceeds 60 mbar. Nitrogen is used as pressure stabilizing gas. A Peltier cooled volume at about -10 °C is placed before the output bubbler. This will recover 70-80 % of the C_6F_{14} vapour in the nitrogen gas. Samples of the liquid can be analyzed with a monochromator before and after cleaning. It has been found that only very small amounts of impurities (oxygen, water) become added to the liquid after the initial flushing of the system with a pure gas.

2.3 Gas radiator

2.3.1 Gas circulation system

Two identical systems [5] provide C_4F_{10} gas[7] to the four 180° segments (fig.5). The pressure in the gas radiator volume is referred to the atmospheric pressure and is controlled to better than 1 mbar. Nitrogen is used as a pressure stabilizing gas. The flow rate in each vessel is ~300 l/h or one volume change every 6-7 h. The system forms a closed circuit with a pneumatically controlled input valve feeding the output compressors.

[4] Nippon Silica Glass Co.
[5] Araldite AW 106
[6] Rohacel
[7] supplier 3M, St.Paul, Min., USA; product code DP L-12321

The differential pressure in the vessels acts negatively on the input valve and positively on the output. The maximally allowed pressure excursion is 1.6 mbar. At the two extreme limits of the domain (underpressure or overpressure) two differential pressure sensors act directly on the compressors. The vessels are protected by large over- and underpressure bubblers. The flow rate is monitored, but not controlled. It is set by the interplay between the input and output pressures.

The gas is maintained clean by flowing it through traps of molecular sieve (13 Å) and activated copper. The copper has not been used in the 1992 run. Nitrogen and other impurities with low boiling points are separated from the C_4F_{10} in a cold trap run at -57 °C. The liquid is then stored and used to fill up the heated (40 °C) pressure vessel which connects to the vessel input valve. The system is controlled by a process controller (see section 2.5).

Gas quality is permanently checked. Ultraviolet transparency is measured with a monochromator. At the current flow rate, the oxygen contamination at the vessel outputs is ~20 ppm, the water content is ~100 ppm. The input gas contains only traces of water and oxygen and shows 100 % UV transmission between 162 and 200 nm. In future, the ratio of N_2 over C_4F_{10} will be monitored by a sound velocity measurement.

2.3.2 Mirrors

The spherical mirrors cover the polar intervals $12° < \theta < 35°$ and $145° < \theta < 168°$ with full coverage in azimuth, except for two 0.1° slices occupied by the side walls of the vessels. The mirrors are arranged in three annuli, each with equal polar coverage of 7.67° . In the inner annulus each mirror covers 30° in azimuth, in the two outer annuli the coverage per mirror is 15° (see fig. 2). This gives a total of 120 mirrors for both endcaps. All mirrors have the same radius of curvature, 120 cm, with the axis pointing towards the intersection point.

The design is a compromise. A small mirror size is in principle preferred, in order to maximize the track length in the gas radiator and because the Cherenkov photons produced by off-axis particles do not form perfect circles in the focal plane. The errors from this deviation, which increases with mirror size, must be small compared to the measurement errors. On the other hand, small mirrors mean that frequently photons from one particle are reflected from more than one mirror, making the reconstruction more difficult. Moreover, more light will be lost in cracks between the mirrors. For practical reasons a number of small deviations from the geometry as described above have been introduced : The mirrors are tilted by a few degrees in order to avoid shadowing by the boxes housing the MWPC preamplifiers, and the mirrors along the side walls of the vessels are smaller to accomodate the wall thickness.

The mirrors were fabricated by slumping floated planar glass plates of 6 mm thickness at about 600 °C in a spherical cast-iron mould. After cutting to the appropriate sizes, the spherical substrates were coated by vacuum deposition of a 50 nm thick layer of Al and a 60 nm thick protective layer of MgF_2. The fabrication method was first developed at CERN and then transferred to industry[8] for the bulk production. More details about the process can be found in [6], which describes the production of the mirrors for the Barrel RICH. Essentially the same process was used for the Forward RICH mirrors.

As described in [6], the reflectivity was measured both by the manufacturer, on small planar glass plates coated together with the mirrors, and subsequently at CERN. At

[8] Bofors Aerotronics AB, Sweden

CERN the reflectivity of each mirror was measured at 15 wavelengths over the range 140-280 nm, using a vacuum ultraviolet spectrophotometer that was large enough to contain the full-size mirror. Fig. 6a shows a typical curve of reflectivity versus wavelength, and in fig. 6b are shown the distributions of mirror reflectivity at wavelengths of 170, 180 and 190 nm. The average reflectivities at these wavelengths are 84.7 %, 87.0 % and 87.2 % and no mirror has reflectivity below 80 %. The shape of a mirror was determined by illuminating the mirror from a point source placed at the centre of curvature of the mirror and measuring the size of the reflected and focused light spot. The manufacturer measured the percentage of light contained inside a circle of 3 mm diameter, corresponding to an angular dispersion of ± 1.25 mrad, which is small compared to the effect of the finite position resolution in the detection plane. On average, 99.3 % of the reflected light was contained within the circle. At CERN the size of the light spot was measured by scanning across it, along perpendicular diameters, with a small photocell. The average observed width of the spot is 0.9 mm. The diameter, where the light intensity has fallen to less than 4 % of the intensity at the centre of the spot, is on average 1.8 mm. These values correspond to angular dispersions of ± 0.38 and ± 0.75 mrad. When the central reflected light spot is shadowed out, inspection of the mirror from its centre of curvature reveals even small imperfections caused by bubbles, indentations or scratches. Whenever such faults together exceeded 0.2 % of the surface area, the mirror was rejected. Such surface faults were the most frequent ground for rejecting a mirror.

Each mirror has its own support, glued to the mirror and mounted in the back plane of the vessel, allowing individual alignment of each mirror. The mirrors can be adjusted in angle and along the z-direction by 3 screws on each support, and also (up to a few mm) with respect to the fixation holes in the back planes of the vessels. The alignment was done with respect to the flange of the vessel, by illuminating each mirror from a point source fixed to the flange and placed at the precalculated centre of curvature of each mirror. The position of each mirror was then adjusted until the light was returned to and focused at the centre. This alignment was done with the vessels open, i.e. without the liquid radiators and driftboxes mounted and, of course, without the final radiator gas.

2.4 Photon detector

2.4.1 Driftboxes

The photon detection plane is subdivided into trapezoidally shaped TPC units. One unit or driftbox (fig. 7) covers a sector of 30°. The drift volume is electrically divided into two symmetrical halves, each read out by a multiwire proportional chamber. The wire chambers are placed along the long sides of the driftbox, i.e. they lie as spokes in the detection plane. The electric field of typically 1 kV/cm is perpendicular onto the chambers. The sides of the driftbox facing the liquid radiators and mirrors are made of UV grade fused quartz plates[9]. The supporting structure consists of glass-fibre-epoxy material (G10). The quartz windows are glued onto a G10 plate, the midwall that divides the drift volume in two halves. The depth of the drift volume varies from 60 mm at the MWPCs to 40-54 mm along the midwall. Two end plates of G10 are glued onto the edges of the windows and the midwall, thus closing the volume on its smaller sides. The MWPCs are housed in pockets made of a sandwich of glass fibre tissue and 2mm of foam. The walls of the pocket are lined with kapton foil to reduce outgassing.

The drift field is established by vacuum deposited NiCr strips, 0.2 μm thick and 150

[9] Nippon Silica Glass Co.

μm wide at 3.0 mm pitch, on both sides of the quartz plates. Metallic strips printed on the endplates are connected to the window strips. A field cage provides further shielding of the drift field from external distortions. It is placed about 25 mm away from the quartz surface and consists of wires at 9 mm pitch. In order to avoid excessive electric fields around these field wires while minimizing their shadow on the detection plane, their diameter varies from 50 μm in the low field region to 200 μm in the high field region.

Strip and wire voltages are supplied by a resistor chain. The HV stability has been tested and no corona ($<$ 100 nA) has been observed in the final geometry and at the operational voltage of 35 kV, which corresponds to 1 kV/cm. The test was done in an atmosphere of 70 % N_2 and 30 % CO_2 with very low concentrations of water and oxygen. Further safety is expected from operating in C_4F_{10}.

The inherent inhomogeneity of the drift field near the midwall of a driftbox is solved by using an ohmic glass voltage interpolator[10]. The potential of the interpolator is fixed every 37 mm. The resistivity of the glass is about $10^{11}\Omega$.cm at room temperature. We have measured the drift distortions by mapping the drift volume using a fine grid single photo-electron source. All distortions are well below the uncertainty expected from diffusion in the drift gas. We observe no significant effect from accumulation of space charge or charging up of the glass and the quartz surfaces, even with a large amount of charge deposited in the drift volume [7].

All quartz plates have been tested [8] for UV transparency: 32 uniformly distributed points on each unit have been measured. The 50 % transparency point is typically between 165 and 170 nm. There is, as expected, a loss in efficiency at joints between quartz plates. This effect has been measured and found to extend over about 10 mm.

Completely assembled driftboxes were also tested for gas leaks. Helium diffusion into the drift volume was found to vary logarithmically with time. The concentration is typically 30-40 ppm of He after 10 days with the normal gas flow rate. This corresponds to a leak rate of about 7×10^{-5} cm^3/sec. Since the perfluorocarbon used as gas radiator is electro-negative [9], we have set a limit of 0.2 ppm admixture of the radiator gas in the drift gas. To make sure that the He test result represents a virtual leak process, part of the detector has been leak tested with a heavier gas (oxygen). No detectable ($<$ 0.5 ppm) variation of the O_2 concentration was found after a two months test.

Since the 1.2 Tesla magnetic field of DELPHI is perpendicular to the electric field in the driftboxes, a fast drift gas implies a large Lorentz angle, which strongly reduces the acceptance for Cherenkov photons from the liquid radiator. (The gas radiator is not affected, because the mirrors focus the light away from inactive regions.) On the other hand, charges must be drifted out of the volume within 10 μs due to the readout multiplexing scheme (see section 3). The choice of drift gas is therefore a compromise between the requirements of a small Lorentz angle, a sufficiently high drift velocity and low diffusion. We have chosen ethane. Measurements of drift velocity and Lorentz angle are described in section 2.4.4.

Charges may also be lost due to diffusion in the gas or due to inhomogeneity of the drift field. Great care has been taken to make the drift field as uniform as possible. The shape of the driftboxes suppresses diffusion losses of charges drifting near the quartz windows: the depth of the drift volume increases from the midwall to the MWPCs (see fig. 7), so that drifting charges are gradually carried further away from the quartz surfaces, without disturbing the spatial coordinates of the charge.

[10] Corning glass 0317

The conversion of UV Cherenkov photons to free electrons is done by adding the photo-ionizing vapour TMAE to the drift gas. The homogeneity of the gas flow through the drift box has been measured. No deviation from homogeneous flow has been observed with TMAE.

2.4.2 Multiwire proportional chambers

The MWPCs for the photo-electron readout are placed at the radial edges of the drift volumes. Two chambers are required per driftbox, leading to a total of 48 MWPC units for the two end caps.

The anode wire and cathode strip addresses and drift time information allow the reconstruction in space of each photo-conversion occurrence. The prime requirement on the MWPC is high sensitivity and good time resolution for signals from both anodes and cathodes. Other features that had to be considered in the MWPC design are suppression of background signals from photons created in the avalanche around the anode wire (feed-back photo-electrons), minimization of electronically transferred crosstalk and operation in a 1.2 Tesla magnetic field. The high degree of crosstalk suppression needed follows from the large dynamic range between the lowest amplitudes of the photo-electron signals and the very large signal amplitudes that are due to charged particles traversing the drift volume.

A cut through the MWPC structure is shown in fig. 8. It consists of two parts, the detection plane and the preamplifier compartment. The MWPC is located in a housing glued to the quartz windows of the drift volume, with the detection plane just in front of the opening between the windows. The housing is open at one end (at the flange of the drift volume) to permit insertion of the MWPC. The electronics compartment extends from the detection plane towards the gas radiator side. This arrangement keeps the amplifiers close to the detection plane, without any significant shadowing of the driftbox quartz window. The gas radiator side is chosen to avoid interception of photons from the liquid radiator side, which may cross a sector boundary.

The detection plane of each MWPC has 320 anode wires at 2.62 mm pitch and 240 cathode strips, 5 mm wide and 42 mm long. The cathode strips are arranged in 20 groups of 12 strips, each group being covered by 16 anode wires. The effective detection area is 841 mm x 60 mm. The mechanical construction of the detection plane is modular, with four modules per MWPC. Each module consists of a 0.3 mm thick printed circuit board glued to a 2 mm thick glass plate over a set of 0.5 mm thick spacers. The 18 μm thick copper layer on the board was first printed with the strip pattern and then polished ($R_a < 0.05$ μm) and plated with gold on nickel. Through-plated holes of 0.2 mm diameter connect the cathodes to soldering pads at the back side of the board. These soldering pads are accessed through a set of holes drilled in the glass plates. The anodes, 20 μm diameter gold-plated tungsten-rhenium wire[11], were applied by winding the wire around the plate in a machine that stepped 2.62 mm after each turn. The height of the anode wire above the cathode plane, 0.7 mm, was assured by ground spacer bars of G10 material. After completion of the winding, the wires were fixed at both ends with epoxy glue[12] and soldered at one end for the electrical connection. The mechanical wire tension of about 0.5 N was verified before accepting a chamber.

The layout of the cathode pattern includes grounded crosstalk-limiting screening strips between the groups of cathode strips, both at the front and at the back side of the

[11] Lumametall, Lumalampan AB, Kalmar, Sweden
[12] Araldite AW 106/ HV 953U

G10 board, with widths of 0.15 mm and 0.25 mm respectively. Dummy strips, 2.5 mm wide, outside the detection region of the MWPC are connected to ground via a 4.7 kΩ resistor (matching the preamplifier impedance) to equalize the stray impedance of the outer and inner active strips in a group. Outside the dummy strips are placed grounded strips (2.5 mm x 209 mm) that are connected to the screening strips. In order to minimize capacitive losses, the cathode strip signals are carried on wires, rather than on a printed circuit board, to their connector in the electronics compartment.

Feedback photo-electron signals are limited by the optical screening structure, fig. 9. This structure is built from two layers of precision-cut screens, made of 0.2 mm thick G10 printed circuit board material. The lower layer has 321 screens, at 2.62 mm spacing, standing centered between the anode wires. These screens are 2.5 mm high and are equipped with two layers of double-sided potential-strips. The upper layer has 25 screens, 4.5 mm high with three potential strips, at a spacing of 2.5 mm. The upper screens are placed on top of, and run perpendicularly to, the lower screens. The upper and lower screen layers are glued together with a small quantity of glue[12]at the 321 x 25 crossing points. The potential strips are 9 μm thick gold-plated copper with a width of 0.15 mm on the lower screens and 0.2 mm on the upper screens. The screening structure is built in two halves, joined together at the centre of the chamber. The screens remove about 80 % of the feedback photons and permit loss-free photo-electron transfer with a fairly low electrical field applied over the structure, also when the 1.2 T magnetic field of DELPHI – parallel to the anode wires – is applied. Crosstalk signals due to pulses created on the electrodes of the screens are reduced by decoupling of both electrode layers on the lower screens. These electrodes are grouped by 16 screens, corresponding to the cathode strip groups, and connected to ground over a 47 pF capacitor and to the voltage bus via a 1 MΩ resistor.

The construction material of the MWPC support structure is DELMAT 68600 [13]. The material was selected after checking that its chlorous content was low, since outgassing of electro-negative substances would lead to loss of drifting photoelectrons. A large ground plane of printed circuit board material covers the bottom plane of the chamber. The TMAE vapour added to the driftgas can easily be oxydized at a copper surface. Therefore, all copper surfaces have been nickel plated. During the final acceptance tests it was verified for each chamber that the total leak rate from the drift volume through the MWPC and its O-ring joints is less than 0.06 mbar × l/hr.

A suitable operating voltage for the anode wires has been determined in tests with single photo-electrons, liberated through ionization induced by UV-light from a hydrogen flash lamp. A plot of anode and cathode counting rates versus anode voltage is shown in fig. 10. An operating voltage of +1650 V on the anodes is seen to give high counting efficiency also on the cathode strips. The cathode strips are kept at ground potential. By iterative optimization in a 1.2 T magnetic field, a set of potentials on the screen electrodes has been determined, where no detectable loss of photoelectrons occurs as compared to the situation without magnetic field. Each chamber was tested for HV stability up to 1950 V.

2.4.3 Driftgas system

The flow diagram of the drift gas system [10] is shown in fig. 11. The drift gas is ethane (C_2H_6) with a small additional fraction of the photo-ionizing vapour TMAE. The

[13] UDD-FIM, DELLE, France

ethane is saturated with TMAE by bubbling it through liquid TMAE in a temperature controlled vessel. The temperature of the bubbler is below that of the detector volume in order to avoid TMAE condensation. The TMAE partial pressure and the absorption coefficient μ (= λ^{-1}) vary as exp(-5614/T) with the absolute bubbler temperature T [4]. Near room temperature this amounts to about 7 % variation per °C.

The driftgas system is referred to atmospheric pressure. This greatly simplifies the system. Still, the absolute pressure must be known to $\pm$0.5 mbar for drift velocity and Lorentz angle corrections. The gas amplification in the MWPCs will also change with pressure, although this effect is not expected to influence the single-electron detection efficiency.

The system is controlled by a process controller (see section 2.5). The differential pressure of the system is maintained to $\sim$0.1 mbar and the temperature of the TMAE bubbler to $\sim$0.1 °C. The system is passively protected against over- and underpressure both at the input and output of the drift boxes. All lines can individually be switched to C_2H_6/TMAE or to N_2. Although individual lines do not have their own flow control, it has been checked that all flow rates are equal to within $\sim$10 %.

The process controller will restart the system after any interrupts, like a power cut or general safety alarm. It will also switch into a safe state if the TMAE temperature or the pressures are too high. A continuous monitoring loop in the process controller ensures the stability of the gas quality. The oxygen and water contaminations as well as the UV transparency can be monitored. There are provisions for installing instruments to measure drift velocity and gas amplification.

Good purity of the output gas (less than 1 ppm of oxygen, about the same for water) can be maintained with a flow rate corresponding to one volume change of the driftboxes per 3 hours. The TMAE temperature has been kept stably at 25 °C, which corresponds to $\lambda \approx 21$ mm at 6.2 eV or 200 nm.

2.4.4 Calibration System

The calibration system [11] is shown in fig. 12 . Ultraviolet light from a lamp is fed into 22 quartz fibres of 100 μm diameter, which project light spots onto the photon detector and allow the determination of drift velocity and Lorentz angle. Further, quartz rods near the MWPCs have a line engraved on their surface to project a line of UV light on the detector in order to monitor all MWPC channels. The engraving of lines on the quartz rods was done with a CO_2 laser. Finally, two alignment fibres near each MWPC allow determination of the MWPC position relative to fiducial marks on the drift volume.

All fibres of a drift volume are placed inside cylinders of G10 material and are mounted on a G10 structure. Each light spot is produced through a 0.5 mm diameter collimator at the end of the cylinder containing the fibre. The G10 frame is mounted on the midwall (see section 2.4.1) of the drift volume. The positions of the light spot centres, measured with 30 μm precision after installation of the fibre systems on the drift volumes, deviate less than 200 μm from their nominal values. The UV lamps are 3-window hydrogen flash lamps developed especially for this system. The lamps are free running at a frequency of 150 Hz when calibration data are taken.

In a calibration run with $\sim$ 100 data points per light spot, one typically obtains wire address coordinates and drift times with errors of about 0.2 mm and 2 ns. From these measurements, the drift velocity v_d and Lorentz angle θ_L are determined by the requirement that the reconstructed positions of the light spots coincide with the nominal

Table 2: Drift velocity and Lorentz angle in ethane at 986 mbar and 30.7 °C in the presence of a crossed magnetic field of 1.2 T.

E_d (kV/cm)	v_d (cm/μs)	θ_L (degrees)
1.03	5.12	49.8
0.97	5.03	51.3
0.94	4.95	51.9
0.88	4.83	53.6
0.81	4.68	55.2
0.75	4.49	56.6
0.69	4.27	58.3
0.63	4.06	59.6
0.57	3.78	60.9

ones. The procedure [11] is to minimize the sum

$$\sum_{allspots} \left[\left(\frac{z_r - z_s}{\sigma_z} \right)^2 + \left(\frac{x_r - x_s}{\sigma_x} \right)^2 \right]$$

where z_r (z_s) and x_r (x_s) are the reconstructed (nominal) positions of the light spots along the directions of drift field and wire address. The drift time offset was determined from a weighted linear fit to the measured times versus the z distance.

Results at our operating point (1.03 kV/cm) and at lower drift fields are listed in table 2. One may correlate the measurements of drift velocity and angle by writing [12] $v_d = \mathrm{k}(\mathrm{E}_d/\mathrm{B})\sin\theta_L$. The factor k, which depends on the velocity distribution and collision cross section of the drifting electrons, is expected to approach a constant value at small drift fields only. In fig. 13 the measured values $\mathrm{k} \equiv v_d \mathrm{B}/(\mathrm{E}_d \sin\theta_L)$ have been plotted against the reduced drift field E_d/N, where N is the number density of the gas. The data points closely follow the calculated curve provided by [13].

2.5 Monitoring and controls

The Forward RICH has been equipped with automated systems for monitoring and control of the physical parameters of the detector. The power supplies for the MWPCs, the drift field and the UV lamp calibration system are controlled and monitored by a G64 microprocessor system [1]. The same system is used to monitor the temperature of the gas radiator and the driftgas, as well as the power supply and the cooling of the preamplifier electronics. The G64 micro processor is connected via thin-wire Ethernet to a VaxStation 4000/60 equipment computer which runs the DELPHI standard slow control software for switch-on of voltages, updating of the calibration data base and display of alarm conditions [14]. The fluid systems are controlled by programmable controllers. Each of the three fluid systems has its own CPU. Two small controllers[14] are used for the drift gas system and the gas radiator system. A fast and accurate control of the pressure inside the liquid radiator is needed because of the small tolerances in relative pressure. This results in a high number (72) of analog pressure meters, which are read out by a larger system[15]. This large CPU is also used to connect all CPU's via a Siemens L1 local area

[14] Siemens Siematic S5-100U
[15] Siemens Siematic S5-135U

network and Ethernet to the equipment computer. The communication is handled by Vax OSI transport service software. Each of the three controller systems runs its own assembler written software, which matches the specific properties of each fluid system. A graphic display of each fluid system allows the display of the settings of the electro-valves, as well as important system parameters such as temperatures, pressures and flow rates. It allows switching between different well-defined states of the system (e.g. normal operation, N_2 purge). Each fluid system is controlled by a process running on the equipment computer that updates the calibration data base for important system parameters and sends alarm messages to the DELPHI Error Message Utility.

3 Electronics and data acquisition

3.1 The electronics chain

The electronics chain [15] is designed to provide digitized time information for signals on each anode wire and cathode strip of the MWPCs. The high number of channels and severe space constraints inside the MWPC volume place strict requirements on simplicity of the circuits and on cost effectiveness of the chain. A high detection efficiency is required for single photoelectrons in the presence of ionizing tracks. The required efficiency is achieved by operating the chambers at a gas amplification in excess of 10^5. In this case, single photoelectrons show a broad Polya distribution of pulse heights near the electronic noise limit, while ionizing tracks have truncated Landau-like distributions. Track segments typically generate 600 primary electrons, distributed over about 10 wires.

Fig. 14 shows schematically the elements of the electronics chain. Preamplifiers are mounted directly in the MWPCs on each wire and strip in assemblies covering 16 wires or 12 strips. They are designed to detect the small single-photoelectron signals, while sustaining the large signals from ionizing tracks with an acceptable dead time. The total number of preamplifier channels is 26,880. The preamplifiers drive the signals through 40 m of shielded twisted pair cable to the rack-based electronics. Each of the 1680 cables carries 16 signal pairs and the supply voltage for the corresponding preamplifier channels.

The signals are received by Amplifier-Discriminator-MUltipleXer (ADMUX2) Fastbus units. Each signal is individually amplified and discriminated against an adjustable threshold. Inside the ADMUX2 units, groups of discriminator outputs are delayed up to three times 10 μs in order to achieve a time multiplexing of the signals at the output. After the delays, the signals appear in four time slots of 10 μs each. This reduces the number of channels by a factor of four, while retaining full acceptance over the 9 μs maximum drift time of the detector. Additional reduction by a factor of two is imposed by a direct ORing of discriminated signals before the delay circuits. There are 420 ADMUX2 modules of 64 input channels each.

The LTD modules [16] complete the electronics chain. These Fastbus modules provide the time digitization relative to an external clock with 10 ns time steps. The total time range of the LTD of 4096 clock pulses is sufficient to cover the four time multiplexing windows. There are 70 LTD modules of 48 channels each. The clock burst provided for the LTD time digitization is also used by the ADMUX2 modules to define the multiplexing delays. The start of the burst is synchronized to the LEP beam cross-over signal (BCO) through the local trigger supervisor unit, PANDORA [17]. The Forward RICH clock module, CKMOD, generates the clock burst from a free running 100 MHz crystal oscillator gated by a signal from PANDORA. While the start of the gate is fixed with respect to BCO, the end might appear after about 3 μs if trigger level 1 is not satisfied, or go to the full 40 μs for accepted events. A series of active Fan-out units distribute the clock to all

ADMUX2 and LTD units.

The adopted scheme of four-fold time multiplexing optimizes the use of the long time window of the LTD. In order to avoid a concentration of hits in a given event in a few LTDs with memory overflows as a result, the cabling has been arranged such that the time multiplexed channels are taken from photon detectors separated by 90° in azimuth (fig. 14). For the same reason, the direct ORing is done between channels from detectors that are 180° apart.

Space points of single photon signals are formed off-line by combining corresponding wire and strip signals that coincide within ±50 ns. With a discrimination threshold corresponding to 15 % of an average photoelectron signal, this time match removes completely the background from uncorrelated electronics noise. By assuring that matching wire and strip channels from one chamber are never ORed together in the same way as a matching pair from another chamber, the ambiguity introduced by the ORing can be fully resolved by the time match criterion.

3.2 Preamplifiers

3.2.1 Present design

The present preamplifier design (Fig. 15) has been optimized for cost, space and power requirements. It is based on a NE592 video amplifier in a surface mount package. The NE592 amplifier has differential inputs and outputs and a 120 MHz unity gain bandwidth, consisting of two internal emitter coupled stages plus an emitter follower output stage. Its voltage gain can be trimmed by an external network up to a maximum value of 400.

The preamplifier works as a voltage amplifier with a 4.7 kΩ resistor connected between one input and ground. The other input is tied directly to ground. In this configuration, the total gain is about 200 with a flat frequency response from 600 kHz up to the NE592 high frequency cut-off. The transfer characteristic causes the differentiation of the long 1/t tail of the input signal and limits the dead time for ionizing track signals to about 1.5 μs. The dead time after single photoelectron signals is very small. The signal delivered at the input of the ADMUX2 module, which is operated at a discrimination threshold of 15 mV, is about 100 mV for an average photoelectron pulse. Anode and cathode preamplifiers are identical except for the high voltage decoupling capacitor on the anode circuits and details in the layout. They are built in surface mount device technology on assemblies which hold 16 anode channels or 12 cathode channels. Each assembly of 40×44 mm^2 consists of two printed circuit boards mounted on top of each other, 2.5 mm apart and with components mounted on the external sides.

The spaces between the circuit boards hold two copper pipes for water cooling, which also provide good common ground bus bars. A fully operating chamber with ±4 V supplied to the preamplifiers dissipates about 50 W of power. Water is circulated through the closed circuit cooling system by pumping a reservoir at the top of the circuit below atmospheric pressure. The underpressure operation prevents water spills in case of leaks in the piping. The temperature inside the MWPC pockets is monitored with Pt-100 resistors. The cooling system is controlled by electronic relays. Status messages are sent to the G64 monitoring system (see section 2.5).

3.2.2 New preamplifier

The signal characteristics and the signal to noise ratio of the NE592 preamplifier are satisfactory for small and medium size pulses. However, due to the limited sink current of

its emitter follower output stage, the negative output signal saturates much earlier than the positive one. The result is unmatched termination for the large signals from ionizing tracks. Although careful optimization of the supply voltage and of the receiver circuit has limited the effect to a 1.5 μs duration, it has prompted us to develop a new type of preamplifier with a shorter dead time.

The new preamplifier, which is currently installed in one quarter of the detector, is designed to have a big dynamic range in order to detect the single photoelectron pulses with good sensitivity and at the same time accept big pulses from ionizing tracks without saturation and long recovery times. It has approximately logarithmic transfer characteristics. To improve the discrimination of small photoelectron signals against noise, the noise performance has been substantially improved compared with the present design. Furthermore, it appeared appropriate to build a current sensitive preamplifier in order to reduce pile-up phenomena in the output signal and decrease the amount of cross talk between adjacent channels.

The new current sensitive logarithmic preamplifier [18] consists of three stages (see fig. 16):

(a) A low noise, high gain, current-to-voltage converter implemented in the classical cascode configuration whose output drives an emitter follower; the feedback resistor provides a relatively low input impedance, of the order of 1 $k\Omega$.

(b) The logarithmic stage is obtained by summing the output currents of two differential amplifiers, each with a different gain, producing an approximately logarithmic transfer characteristic.

(c) The output stage is implemented in such a way as to give a symmetrical balanced output driving at least 40 mA into a 100 Ω twisted pair cable.

Each channel of the new preamplifier absorbs about 8 mA from the +6 V supply and about 9 mA from the -6 V supply. The frequency response is flat within 3 dB from a few MHz to about 35 MHz. The output amplitude for an average photoelectron signal is about 60 mV. The output noise is approximately gaussian and has an effective r.m.s. value of about 3.2 mV for the full differential anode swing (cathodes show a similar figure), which allows us to lower the discrimination threshold to 5 mV. The recovery time after injection of a 1200 fC pulse, which is representative of an ionizing particle signal, is $\approx$500 ns. Fig. 17 shows the efficiency for detecting a 3 fC pulse, which simulates a photoelectron signal, after a 1000 fC pulse charge, as a function of the time separation between the two signals.

The preamplifiers have been implemented as thick-film hybrid circuits. Each hybrid has dimensions of $38 \times 10 \times 2.5$ mm^3. The hybrid circuits are stacked at a 0.1 inch spacing on a multilayer printed circuit board on which both the high voltage capacitors needed for the coupling with anodes and the power supply filtering capacitors are soldered. The gain uniformity of both anode and cathode circuits has been measured to be better than 10%.

3.3 The ADMUX2 module

The ADMUX2 module is described in detail in [15]. The module consists of three parts: the Fastbus mother board, 16 discriminator daughter boards, and an auxiliary card common to two neighbouring ADMUX2 modules. Each ADMUX2 performs a discrimination of the 64 differential analog inputs. The discriminator circuit diagram is shown in fig. 18. Thresholds from 4 mV to 50 mV are defined by DACs on the mother board in groups of 8 channels. No detectable cross-talk has been seen at the minimal threshold due

to careful design of the circuit layout and properly distributed by-pass capacitors. Each input channel can be individually disabled to block off noisy channels.

The discriminated signals from neighbouring input connectors are then ORed, in order to reduce the channel count to 32. In two groups of 16 channels the signals are then delayed by a selectable multiple of the external clock cycle (set to 1000 cycles of 10 ns) and joined on the output connector, now carrying 16 channels. The module can by switch selection be configured in either of two modes. In the low-mode configuration, the first 16 channels are driven directly to the output while the other 16 channels are stored in the circular memories, waiting for time slot 2 (10–20 μs) before going to the same output. High-mode units store all signals in memory and shift the output by two time slots compared to the low-mode ones, so the outputs appear in time slots 3 (20–30 μs) and 4 (30–40 μs).

The OR and multiplexing logic and the Fastbus communication logic to set enable masks and thresholds in Control Status Registers is placed on the mother board. The multiplexing uses a 1 k word shift register implemented in fast ECL static memories, sequentially addressed by a pointer to work in a circular configuration and clocked by the 100 MHz external clock.

The full four-fold time multiplexing is achieved by placing a low- and a high-mode unit in adjacent slots in the Fastbus crates and combining the outputs on the auxiliary card, see fig. 14. The auxiliary card consists of two printed circuit boards, mounted one on top of the other and connected together by an internal connector. It is plugged into the two adjacent slots of the Fastbus auxiliary area and performs an OR of the single-ended signals coming from two mother boards, before converting them into differential signals driven onto a twisted pair flat cable. The mother board also provides the ± 5 V power for the preamplifiers through a few wires of the 40 m cable. The power is derived from the ± 15 V line of the Fastbus power supply and can be disabled by a Fastbus command.

3.4 Data acquisition

The DELPHI data acquisition system is described elsewhere [1, 19]. The Forward RICH Fastbus system forms two partitions of this system, one for each endcap. In addition to the LTD modules, each endcap system contains a local trigger supervisor, PANDORA, and a Fastbus Intersegment Processor (FIP) for readout control.

For accepted events, the data is stored in the four event deep front-end buffers in the LTD modules. The FIP is programmed to transfer the raw data from all LTD modules into its memory and format the event. From here the events are either injected into the general DELPHI data stream through Fastbus or transferred to a VaxStation 4000/60 computer through Ethernet for local analysis. The latter mode of operation is used for tests and calibration runs. The local data stream can also be activated during general DELPHI data taking in order to spy on the Forward RICH data. Online data analysis consists of processing of calibration data in order to extract drift velocities and Lorentz angles for each photon detector as well as quality checking of the data during standard LEP running.

4 Performance

4.1 Photon yield from C_6F_{14}

The number of Cherenkov photons emitted per unit of wavelength and per unit of pathlength in the radiator is $(2\pi/137)\sin^2\theta(\lambda)/\lambda^2$. The Cherenkov angle θ depends on the wavelength λ due to chromatic dispersion in the C_6F_{14} liquid. When a particle

with velocity $\beta \approx 1$ traverses one cm of C_6F_{14}, the photons emitted will on average pass through 0.6 cm of C_6F_{14} and 1.4 cm of quartz. They also cross an average depth of 26 cm of C_4F_{10} gas before arriving at the photon detector, because the space between the liquid radiator and the drift boxes is in open contact with the gas radiator volume. Fig. 19 shows the variation with wavelength of the transmission in C_6F_{14}, in quartz and in C_4F_{10} gas [16], and the transmission after two reflecting quartz surfaces. Multiplying the resulting total transmission — weighted with the variation in photon emission with wavelength — with the TMAE quantum efficiency, the spectrum of observable photons is obtained. It is limited at short wavelength by absorption in C_6F_{14}, while the TMAE quantum efficiency sets the higher limit.

For our radiator thickness of 1 cm, 27.0 photoelectrons would be created in a geometrically unlimited photon detector. The average wavelength of the Cherenkov photons is 193.1 nm.

The acceptance for C_6F_{14} photoelectrons is limited geometrically by the finite radial dimensions of the photon detector and by the non-sensitive regions that house the MWPCs. The Lorentz effect also reduces the acceptance, since photoelectrons created in certain areas can not be driven to the chambers. Finally, the acceptance for photon detection is reduced because a part (up to one half) of a Cherenkov cone can be obscured by other C_6F_{14} containers. The net geometrical acceptance varies between 0.2 and 0.6 with a mean value of 0.44, thus reducing the number of observable photoelectrons to 11.9.

In order to enhance the signal/noise ratio, the off-line pattern recognition will use only the signals from the nearest 2/3 of the photon detector depth, which varies between 4 and 6 cm. With this selection rule and assuming a TMAE temperature of 25 °C, 85.5 % of the signals will be used in the analysis, giving 10.2 photoelectrons/ring.

Table 3: Number of photoelectrons from the liquid radiator for a $\beta \approx 1$ particle (simulation).

Photon yield from C_6F_{14}	photons	photons
Photoelectrons in unlimited detector		27.0
Outside geometrical acceptance	15.1	
Photoelectrons not detectable	1.7	
Deadtime losses (estimated)	0.5	
Detectable photoelectrons		9.7
Found in pattern recognition		9.3
Photoelectrons from C_6F_{14}	8.90	
Feed back photons	0.25	
Photoelectrons from C_4F_{10} gas	0.15	
From quartz window and ionizing tracks	0.01	

Due to electronics dead time, part of the electrons are not detected. To arrive at an estimate of dead time losses, a survey was made of which signals are found in front of a genuine C_6F_{14} photoelectron signal in a given anode or cathode electronic channel. Fig.

[16] For gas sampled at the vessel output before the purifier. Numbers for clean C_4F_{10} are given in table 1.

20 shows that most of the deadtime losses are caused by other C_6F_{14} signals and most of the remaining losses are due to feedback photons from the C_6F_{14} signals. Estimating the effective deadtime to be 250 ns, 2.5% of the anode signals and 5% of the cathode signals will be lost. Since these losses are highly correlated, the number of detectable signals must be reduced by 5%. The expected number of detectable photoelectrons thus becomes 9.7 per saturated Cherenkov ring. As shown in table 3, the average number of photoelectrons found by the pattern recognition program in simulated events is 9.3 for a $\beta \approx 1$ particle, which includes 0.4 photoelectrons from background sources.

Experimentally, an average of 7.8 photoelectrons per track is observed within a $\pm 3\sigma$ band around the Cherenkov peak from 45 GeV/c muons.

4.2 Photon yield from C_4F_{10}

The number of Cherenkov photons emitted per cm in the C_4F_{10} gas radiator varies likewise with wavelength. When a particle at light velocity traverses 60 cm of C_4F_{10}, the emitted photons will on average pass through 90 cm of C_4F_{10} and 0.6 cm of quartz. Fig. 21 shows the transmission in C_4F_{10} and in quartz, the transmission after reflection in one quartz surface and the reflectivity of the spherical mirrors. The spectrum of observable photons is obtained by multiplying the resultant total transmission, weighted by the variation in photon transmission, with the TMAE quantum efficiency. The photon window is limited at short wavelength by absorption in C_4F_{10} and quartz, while TMAE quantum efficiency sets the limit at long wavelength.

Collecting Cherenkov photons emitted over the 60 cm of radiator depth, 17.1 photoelectrons would be created in an unlimited photon detector. The average wavelength of the Cherenkov photons is 189.7 nm.

The acceptance for detecting photons from the gas radiator can be geometrically limited by the boxes containing the MWPC electronics. The Lorentz effect also somewhat reduces the acceptance. Most ($\approx 2/3$) of the C_4F_{10} Cherenkov rings are not limited geometrically. The net geometrical acceptance is 0.815, thus reducing the average number of observable photoelectrons to 13.9.

Using the above mentioned pattern recognition selection rule and assuming a TMAE temperature of 25 °C, 84 % of the signals will be used in the analysis, leading to 11.7 photoelectrons per ring.

An estimate of the signal losses from deadtimes can be obtained from a survey of which signals are found in front of a genuine C_4F_{10} photoelectron signal in a given anode or cathode channel. Fig. 22 illustrates that most of the deadtime losses are caused by other C_4F_{10} signals. Other losses are due to feedback photons and ionizing track signals. Estimating the effective deadtime to be 250 ns, 11% of the anode signals and 15% of the cathode signals will be lost. Since these losses are highly correlated, the number of detectable signals is reduced by 15%. The expected number of photoelectrons thus becomes 9.9 per saturated Cherenkov ring.

The number of photoelectrons reconstructed by the analysis program in simulated events is 10.1, of which 8.4 originate from Cherenkov photons emitted in the gas radiator. The contributions from various background sources are given in table 4. Experimental data for 45 GeV/c muons contain an average of 10.9 photoelectrons per track within a $\pm 3\sigma$ band around the mean Cherenkov angle. A fit to signal and background terms classifies 8.7 of these as signal, 2.2 as background.

Table 4: Number of photoelectrons from the gas radiator for a $\beta \approx 1$ particle (simulation).

Photon yield from C_4F_{10}	photons	photons
Photoelectrons in unlimited detector		17.1
Outside geometrical acceptance	3.2	
Photoelectrons not detectable	2.2	
Deadtime losses (estimated)	1.8	
Detectable photoelectrons		9.9
Found in pattern recognition		10.1
Photoelectrons from C_4F_{10}	8.4	
Ionizing track feedback photons	0.5	
From quartz window	0.3	
Other feedback photons	0.2	
Photoelectrons from C_4F_{10} gas	0.2	
Ionizing track signals	0.2	
From other sources	0.2	

4.3 Resolution on Cherenkov angle

An important condition for a high resolution in Cherenkov angle is to have corresponding anode and cathode signals in narrow time coincidence. Since the cathode signal has smaller amplitude than the anode signal, time slewing will produce a time difference. Fig. 23a shows the time match of anode versus cathode signals for a sample of the 1992 data. The peak is well centered (+1.3 ns) with an r.m.s. value of 15 ns. Position and width of the peak are almost identical to the result from simulation (fig. 23b), which proves the proper functioning of the OR-ing and multiplexing encoding and decoding in hardware and software.

From simulation, where all modules function to perfection and the alignment of all components is ideal, the position uncertainty in track reconstruction at the Forward RICH detector is found to be 0.6 mm. In actual data, the displacement of the observed track segment relative to the track extrapolation can be studied through a simple pattern recognition used in alignment studies. The position variation of these ionizing track signals amounts to about 1.3 mm, a number that includes uncertainties in track fit and extrapolation, including misalignment and miscalibration of track detectors and of the Forward RICH detector itself.

The main error in Cherenkov angle determination is due to the uncertainty in space point reconstruction in the photon detector, with contributions from anode wire spacing (as wirespacing/$\sqrt{12}$), cathode strip width (as width/$\sqrt{12}$), drift time resolution (a convolution of time digitizer binning and signal rise time) and diffusion over the drift length. In the analysis the Cherenkov photons are treated as monochromatic with the average wavelength. This necessary procedure introduces an error of 3.3 mrad/photoelectron for C_6F_{14} and 0.4 mrad/photoelectron for C_4F_{10}. The uncertainty in the track extrapolation contributes an error of 0.4 mrad in both cases; for C_6F_{14} it originates from track position uncertainty, for C_4F_{10} from the error on track direction.

The average r.m.s. error assigned in the analysis of simulated signals is 7.5 mrad/photoelectron for C_6F_{14} and 2.4 mrad/photoelectron for C_4F_{10}. When analyzing such simulated tracks,

actually obtained values are 9.0 mrad/photoelectron in C_6F_{14} and 2.8 mrad/photoelectron in C_4F_{10}, as illustrated in fig. 24. The error assignments in the analysis of real data are similar to the errors assigned in Monte Carlo studies, but with an influx of larger errors from space points formed from anode/cathode multi-hit clusters. The average error assignment per photoelectron is 8.8 mrad for C_6F_{14} photons.

In the analysis of C_6F_{14} signals in events where an isolated 45 GeV/c muon traversed the detector, the actually observed resolution is $\sigma(\theta_C) = 11.2$ mrad/photoelectron, see fig. 25. This value is slightly larger than is expected from the Monte Carlo studies. The difference may partly be due to insufficiencies in the simulated detector response leading to a too optimistic expectation, but it should also be noted that the calibration and alignment procedures for the detector elements have not yet reached their final form.

Analyzing the C_4F_{10} signals from 45 GeV/c muons, the result $\sigma(\theta_C) = 3.5$ mrad/photoelectron is obtained, see fig. 26. Again, it is expected that the simulation result of 2.8 mrad/photoelectron will be approached when alignment and calibration become perfected.

4.4 Particle identification

The particle identification is performed by the RICH analysis code [20], a common package for the Barrel RICH and Forward RICH which is part of the DELPHI event analysis software. The main steps in the procedure are:

- form point clusters by combining signals at about the same drift time in neighbouring anode or cathode channels.
- search for pairs of anode and cathode clusters that coincide within a narrow time window - this procedure will in general resolve ambiguities from the OR'ing scheme. Form space points from the drift time and the anode and cathode positions in the local MWPC coordinate system. Transform the coordinates from the local frame to the global DELPHI coordinate frame.
- for each track to be analyzed, collect space points in the part of the detector that can be reached by photons from the track particle (fast pattern recognition neglecting refractions).
- perform an iterative fit to obtain the precise emission angle relative to the track direction for each point (detailed pattern recognition, taking refractions into account).
- exclude parts of the azimuthal projection where the found number of points significantly exceeds the expected number, in order to minimize structured background.
- compute the geometrical acceptance for each mass hypothesis and establish the expected number of photoelectrons as well as the background level.
- perform a maximum likelihood fit for 5 mass hypotheses (e, μ, π, K, p) for points selected for C_6F_{14} analysis as well as for the C_4F_{10} points.
- finally, combine the findings from the two fits and present the result as relative probabilities for the 5 mass hypotheses.

This program chain has been used in the studies of photon yield and resolution (sections 4.1–4.3). These studies have been performed on single, isolated tracks of high momentum, where the expected Cherenkov angle approximates the maximal Cherenkov angle (at β=1). In Monte Carlo simulation, however, the true particle identity is known and the identification capability of the analysis program can be studied as a function of particle momentum, see the identification charts for the Forward RICH in [21]. As an example, fig. 27 shows the capability of identifying simulated kaons superimposed on a heavy jet background.

In analyzing multi-track hadronic events in real data, the true particle identity is in general unknown. Fig. 28 displays experimental data from hadronic Z^0 decays obtained with the liquid radiator. A clean separation between pions, kaons and protons is realized.

5 Conclusions

The Forward RICH detector of the DELPHI experiment is now operational. Pilot operation of one quarter of the system has shown that all components function reliably. It has been found worthwhile to increase the dynamic range and signal-to-noise ratio of the preamplifiers.

In each of the two radiator media, the number of detectable photons per particle is about 10 at $\beta \approx 1$. First results on the resolution in Cherenkov angle indicate that values close to the simulation prediction will be obtained once calibration and alignment procedures become perfected.

Combined with efficient track reconstruction in the forward regions of DELPHI, the good intrinsic performance of the Forward RICH detector opens the possibility to select samples of hadronic Z^0 decays that are enriched in a specific primary quark flavour. Leading kaons constitute an efficient tag for $Z^0 \to s\bar{s}$ events, while selection of leading protons and pions leads to enrichment in primary u and d quarks. Forward RICH data will especially contribute to the measurement of flavour-specific forward-backward asymmetries. In the future LEP runs at high energy the study of two-photon physics will also benefit substantially from particle identification at low polar angles.

Acknowledgements

We thank our colleagues of the DELPHI collaboration for their support of the Forward RICH project. Special thanks are due to the members of the on-line group for their flexibility during the start-up phase of the detector. Development of the RICH off-line software has been a common effort with colleagues of the Barrel RICH project; we are especially indebted to P.Baillon, D.Bloch and I.Herbst as primary authors of the analysis and simulation codes and to M.Berggren for his valuable software alignment package. The dexterity with which C.Brand and his group addressed the cooling of the preamplifiers and their work on the photon screens are gratefully acknowledged, as well as the skillful work of K.Ley on the recirculation system for the liquid radiator. We are much indebted to F.Formenti for his work on the ADMUX2 modules. The advice of M.Bosteels during the development of the fluid systems and of the MWPC cooling system has been very profitable. We thank D.Bernier for his contributions to the mechanical design of the detector. The work of S.Ilie on the fluorocarbons is gratefully acknowledged. We are indebted to P.Kokkinias for his effort on the slow controls. Many more technical collaborators at the participating institutes and at CERN have with dedication contributed to the project. We wish to express our gratitude and appreciation to all of them.

References

[1] P.Aarnio et al. (DELPHI Collaboration), Nucl.Instr.Meth. A303(1991)233.

[2] J.Séguinot and T.Ypsilantis, Nucl.Instr.Meth. 142 (1977) 377;
J.Séguinot et al., Nucl.Instr.Meth. 173 (1980) 283;
T.Ekelöf et al, Physica Scripta 23 (1981) 718;
E.Barrelet et al., Nucl.Instr.Meth. 200 (1982) 219.

[3] L.O.Eek et al.,IEEE Trans.Nucl.Science NS-31 (1984) 949;
W.Dulinski et al., Nucl.Instr.Meth. A252 (1986) 418;
P.Beltran et al., Proc.Int.Symp. on Position Detectors in High-Energy Physics, Dubna, 1987, JINR D1-13-88-172, p.286;
R.Arnold et al., Nucl.Instr.Meth. A252 (1986) 188;
R.Arnold et al., Nucl.Instr.Meth. A270 (1988) 255;
R.Arnold et al., Nucl.Instr.Meth. A270 (1988) 289;
O.Botner et al., Forward RICH Review Report, DELPHI 88-7 GEN 73/ RICH 30, February 1988;
E.G.Anassontzis et al., Nucl.Instr.Meth. A323 (1992) 351.

[4] D.F.Anderson, Nucl.Instr.Meth. 178 (1980) 125;
R.Apsimon et al., Nucl.Instr.Meth. A241 (1985) 339;
R.A.Holroyd et al., Nucl.Instr.Meth. A261 (1987) 440;
R.A.Holroyd et al., J.Phys.Chem. 89 (1985) 4244.

[5] C.Barnoux et al., Station d'Alimentation du Radiateur Gazeux du Forward RICH de DELPHI, Internal Report ISN Grenoble, November 1991.

[6] P.Baillon et al., Nucl.Instr.Meth. A277 (1989) 338.

[7] B.Boštjančič et al., Nucl.Instr.Meth. A323 (1992) 363.

[8] J.J.Garcia, Report on the Forward RICH Drift Box Transparency Measurements, DELPHI Forward RICH note, April 19, 1991.

[9] D.Fraissard et al., Nucl.Instr.Meth. A252 (1986) 524.

[10] G.Cerutti and A.Robohm, The Forward RICH Drift Gas System, DELPHI Forward RICH note, August 26, 1992.

[11] A.Markou et al., Determination of Drift Velocity and Lorentz Angle in the Forward RICH, DELPHI 91-95 RICH 45, October 1991.

[12] A.Breskin et al., Nucl.Instr.Meth. 124 (1975) 189.

[13] B.Schmidt, private communication: calculation from ethane cross sections (unpublished) using a multi-term solution of the Boltzmann equation for crossed E and B fields, see K.F.Ness, Phys.Rev. E47 (1993) 327.

[14] T.Adye et al., Comp.Phys.Commun. 57 (1989) 466.

[15] P.Dam et al., Design and Performance of the Readout Electronics Chain of the Delphi Forward Ring Imaging Cherenkov Detector, IEEE Trans.Nucl.Science NS-39 (1992) 1292 and DELPHI 91-98 RICH 46/ ELEC 36.

[16] G.Delavallade and J.P.Vanuxem, Nucl.Instr.Meth. A252 (1986) 596.

[17] S.Cairanti et al., PANDORA: The DELPHI Local Trigger Supervisor Control Box, User Manual, DELPHI 89-12 DAS 92.

[18] F.Fontanelli, V.Gracco, F.Montano and M.Sannino, Progetto di un front-end a risposta logaritmica per un rivelatore Rich, Report INFN/AE-92/15.

[19] W. Adam et al., The DELPHI Fastbus Readout System, CHEP conference, Tsukuba, March 11–18, 1991;
T. Adye et al., Architecture and Performance of the DELPHI Data Acquisition and Control System, idem.

[20] P.Baillon, Nucl.Instr.Meth. A238 (1985) 341.

[21] O.Botner and E.Dahl-Jensen, Physics with the Forward RICH (Contribution to the Workshop on the Future of DELPHI, February 1992), DELPHI 92-167 RICH 94.

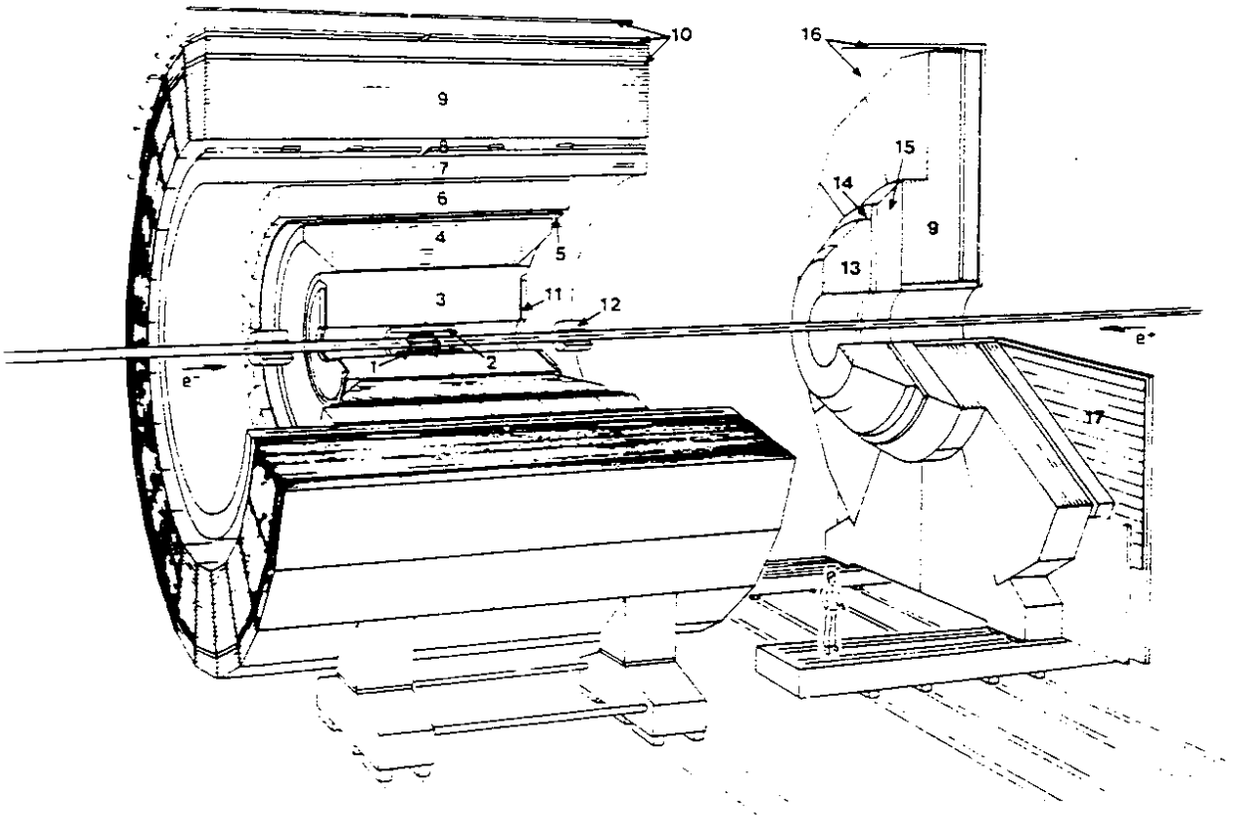

Figure 1: View of the DELPHI detector assembly; 1 = microvertex detector, 2 = inner detector, 3 = time projection chamber, 4 = BARREL RICH, 5 = outer detector, 6 = electromagnetic calorimeter, 7 = solenoid, 8 = time-of-flight counters, 9 = hadron calorimeter, 10 = muon chambers, 11 = forward chamber, 12 = luminosity monitor, 13 = FORWARD RICH, 14 = forward chamber, 15 = electromagnetic calorimeter, 16 = muon chambers, 17 = scintillator hodoscope.

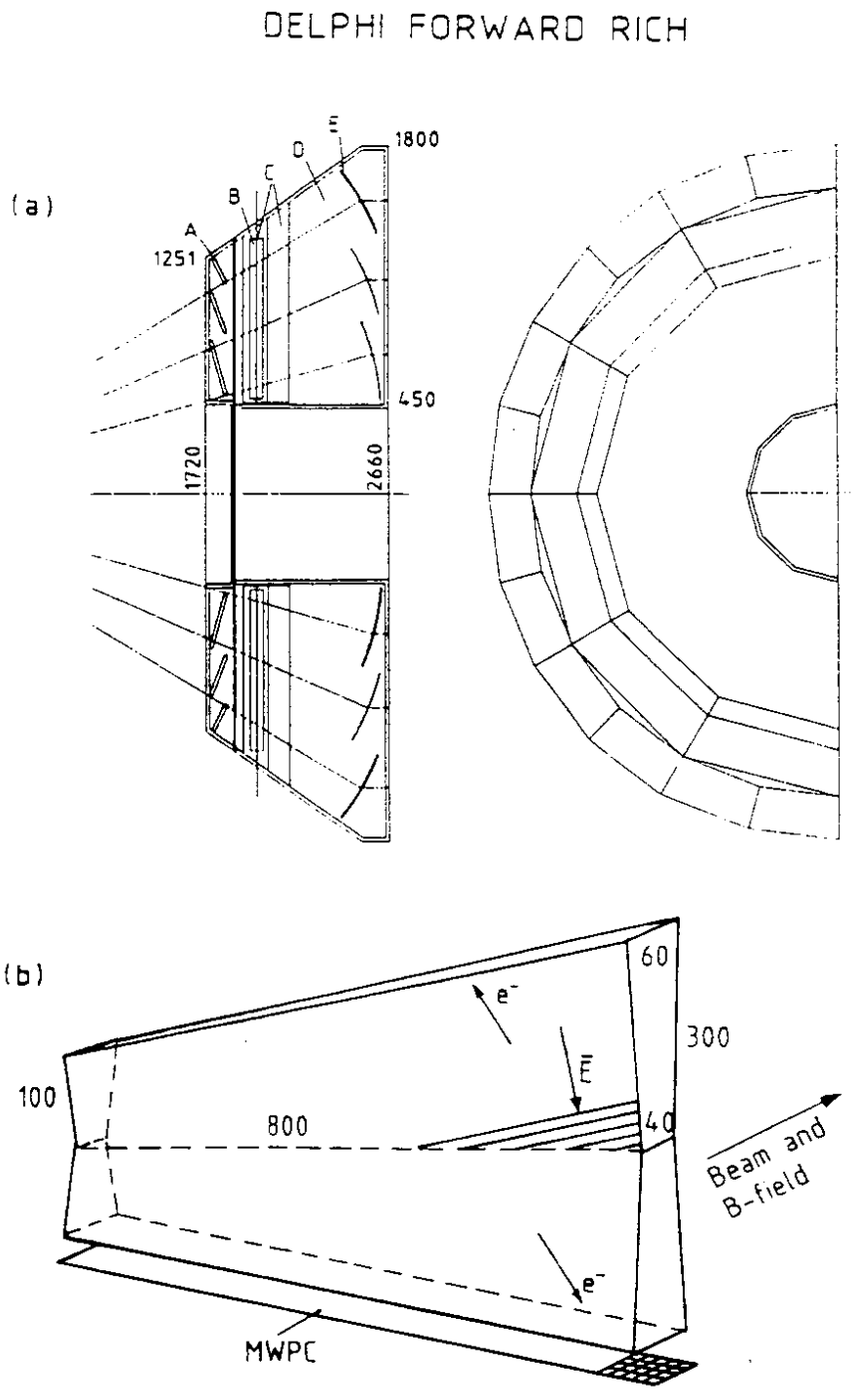

Figure 2: Arrangement of the Forward RICH components. (a) Layout of half an endcap: A = liquid radiators, B = drift volume, C = MWPC, D = gas radiator, E = mirrors. (b) Drift volume covering a 30° sector.

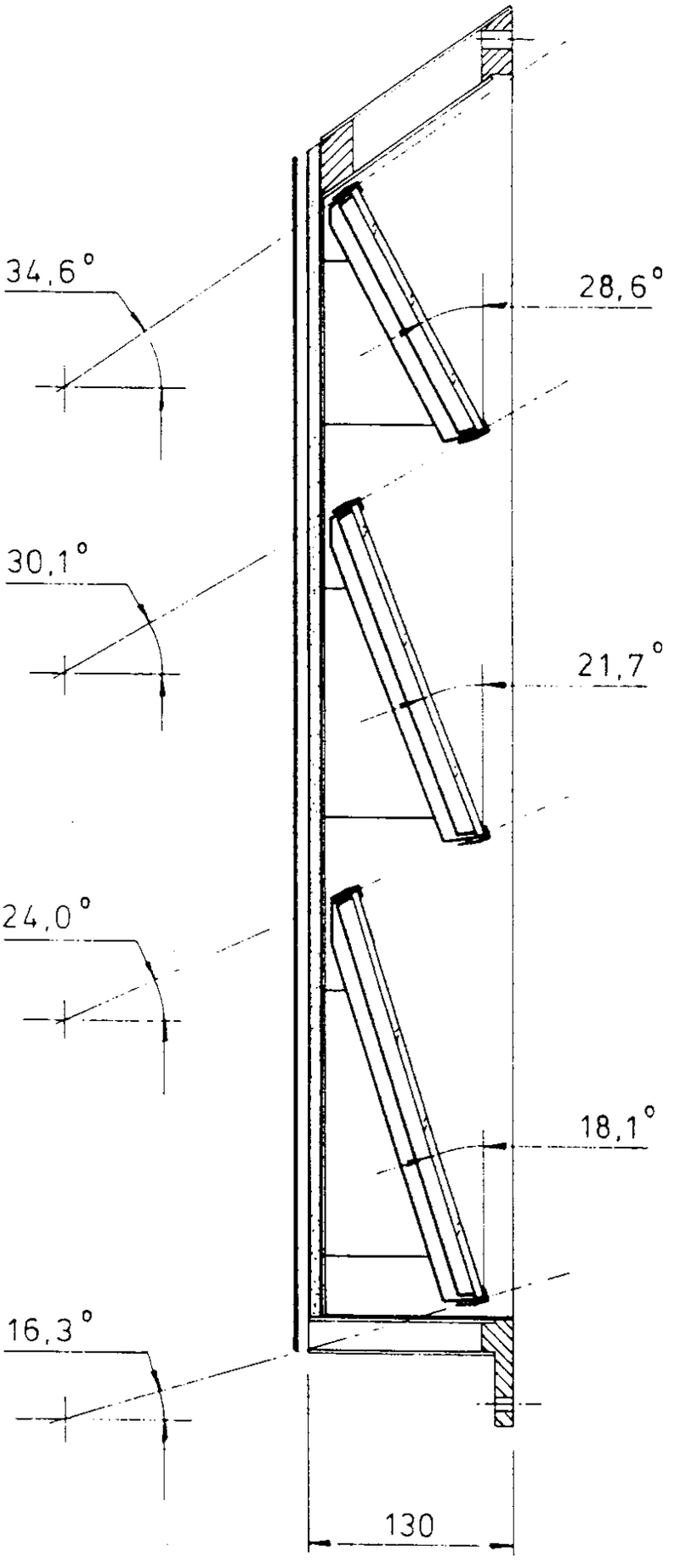

Figure 3: Cross section through the liquid radiator plane.

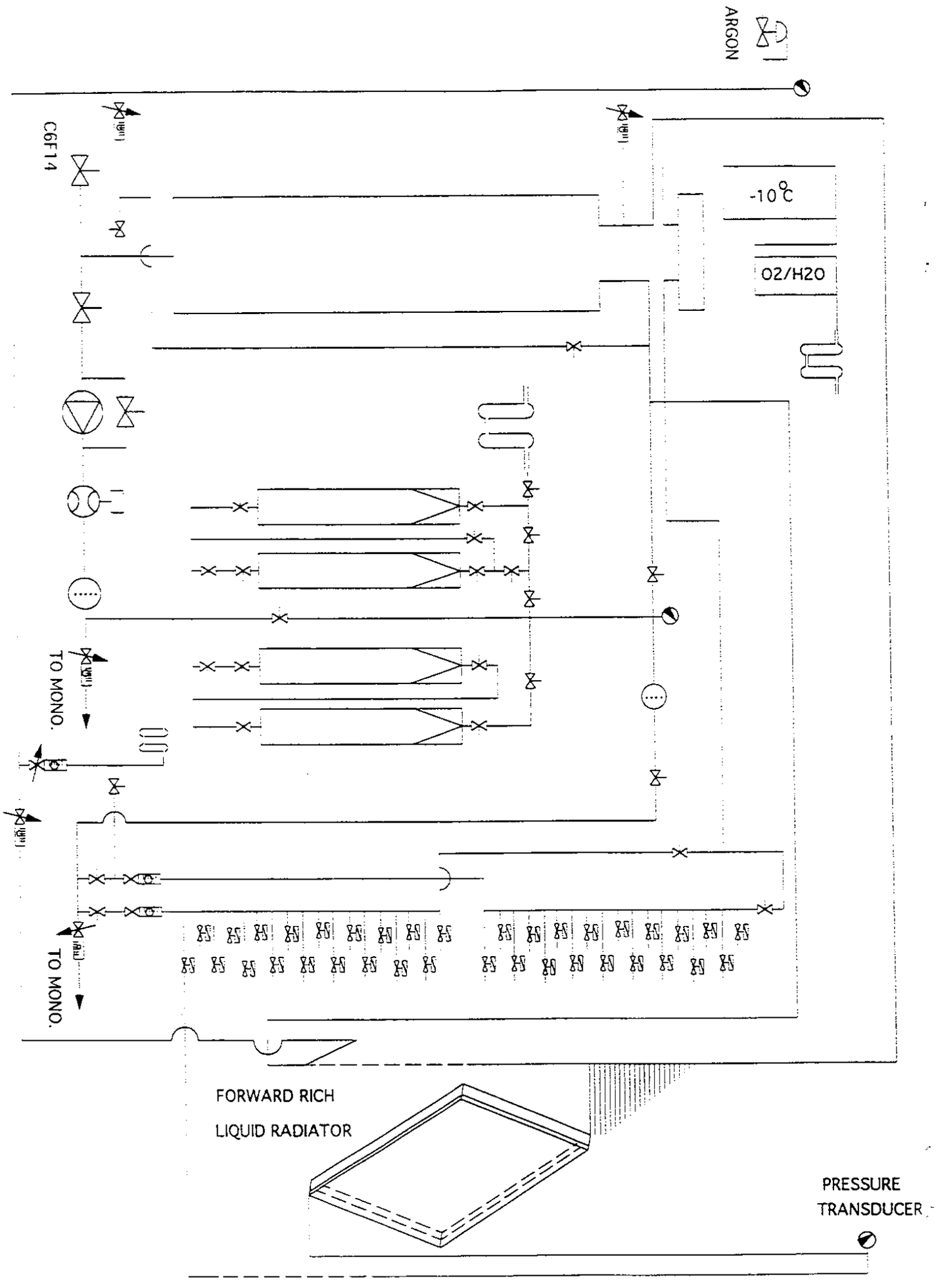

Figure 4: The C_6F_{14} liquid radiator circuit.

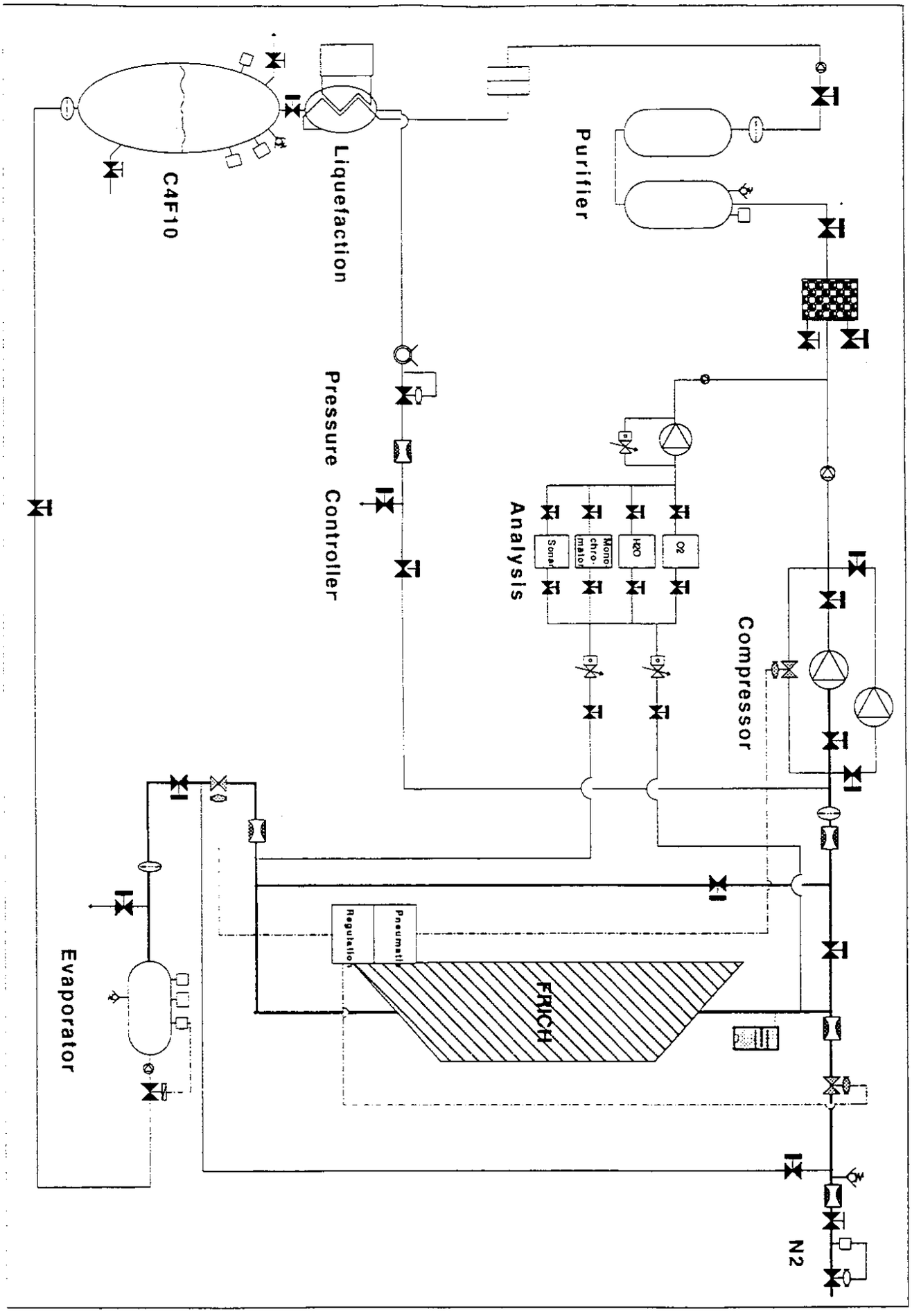

Figure 5: The C_4F_{10} gas radiator circuit.

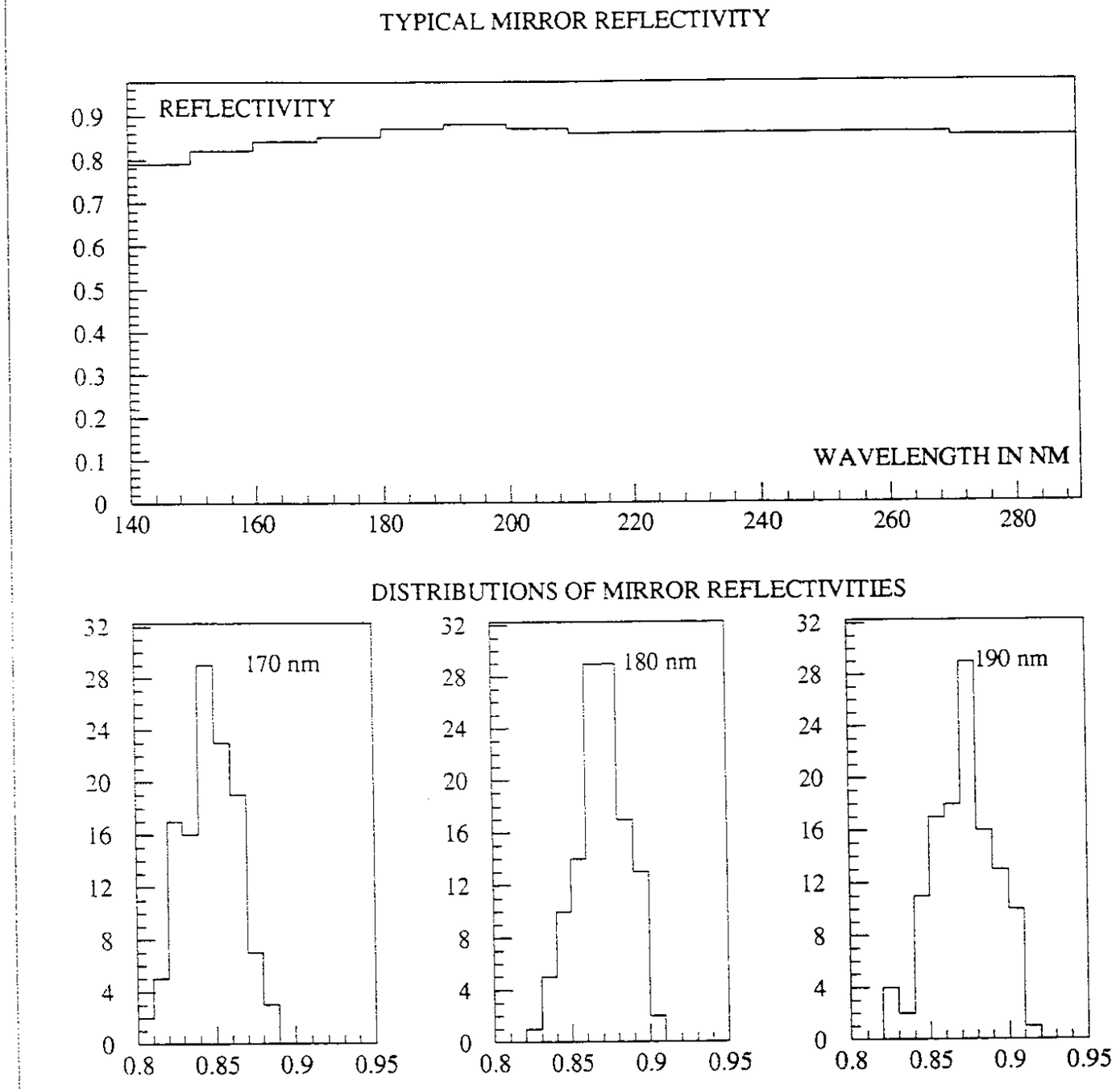

Figure 6: Mirror reflectivity versus wavelength (a) and reflectivity distributions at 170, 180 and 190 nm (b).

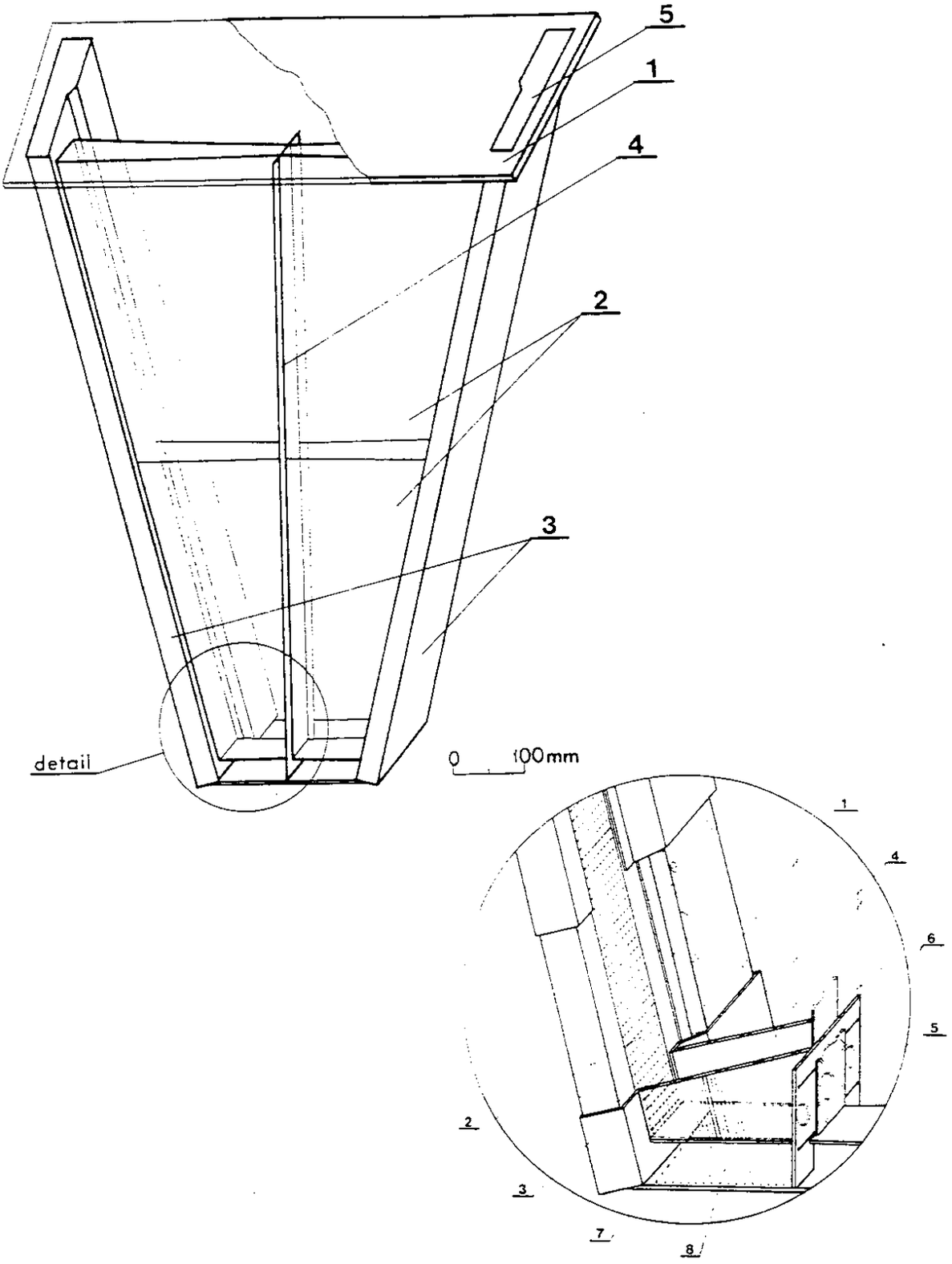

Figure 7: Perspective view of the photon detector: 1 = outer support flange; 2 = quartz plates; 3 = housing of the MWPC; 4 = midwall; 5 = opening for MWPC insertion. The detailed view shows: 1 = electronics compartment of the MWPC; 2 = photon screens of the MWPC; 3 = the MWPC housing glued to the quartz; 4 = quartz plates; 5 = midwall; 6 = resistive glass voltage interpolator; 7 = NiCr strips on quartz; 8 = field cage wires.

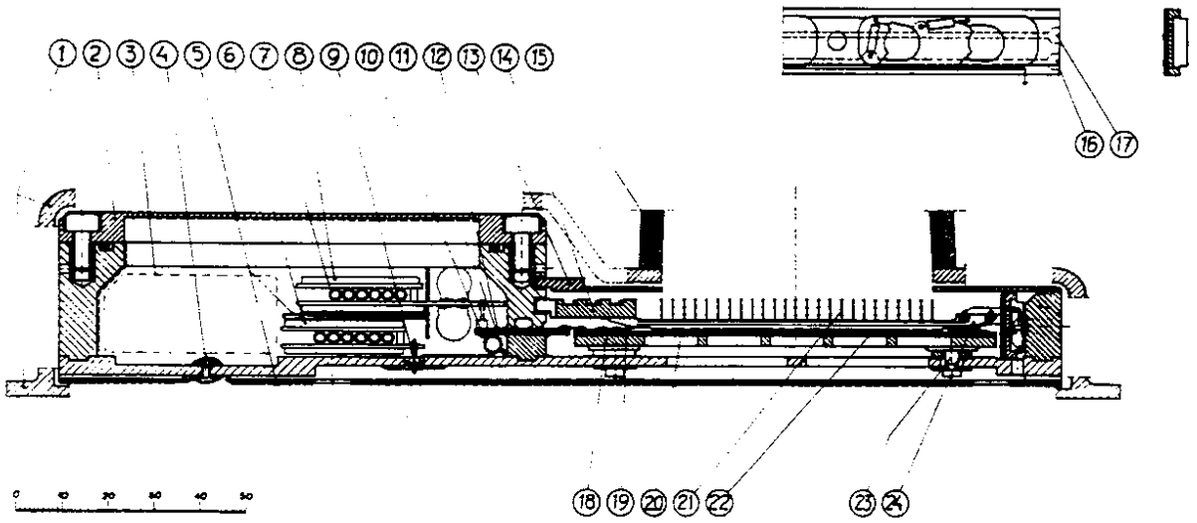

Figure 8: Cut through an MWPC module: housing (1); electronics compartment lid (2); preamplifier cables (3); copper screening layer (5) and feed-through (4); cathode (6) and anode (8) preamplifiers; cooling pipes (7); feed-throughs for anode (12) and cathode (9) signals; nitrogen flushing (10); test pulse antenna (11); protection frame (13); support frame (14); drift box quartz windows (15); detail of outer support frame with voltage busses (16 and 17) for photon screen electrodes; glass support plate (18) for cathode board (22); spacer (19) for anode wire (20) with adjustable fixation (23); upper (21) and lower (24) photon screens. The reference scale is in millimeters.

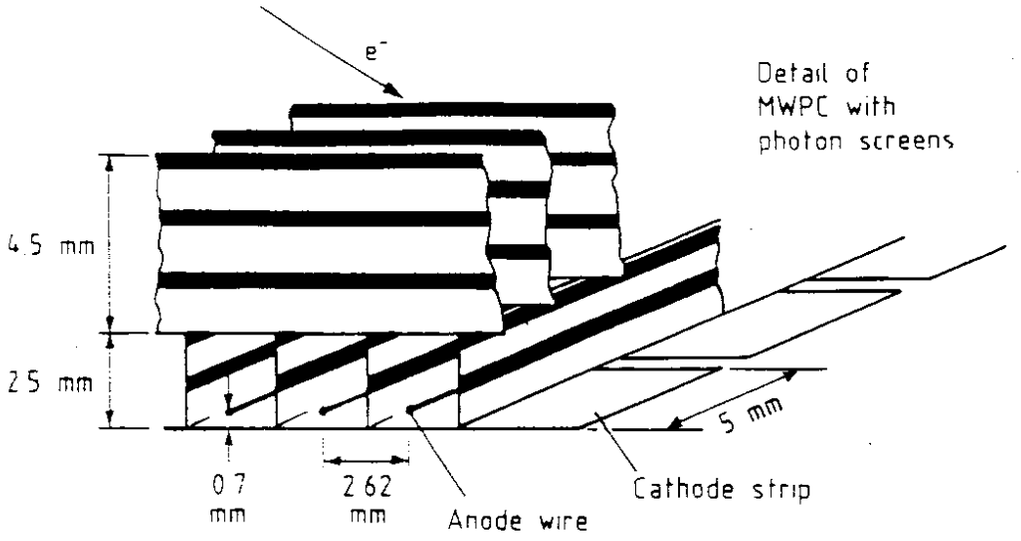

Figure 9: The structure of photon screens for the suppression of feedback signals.

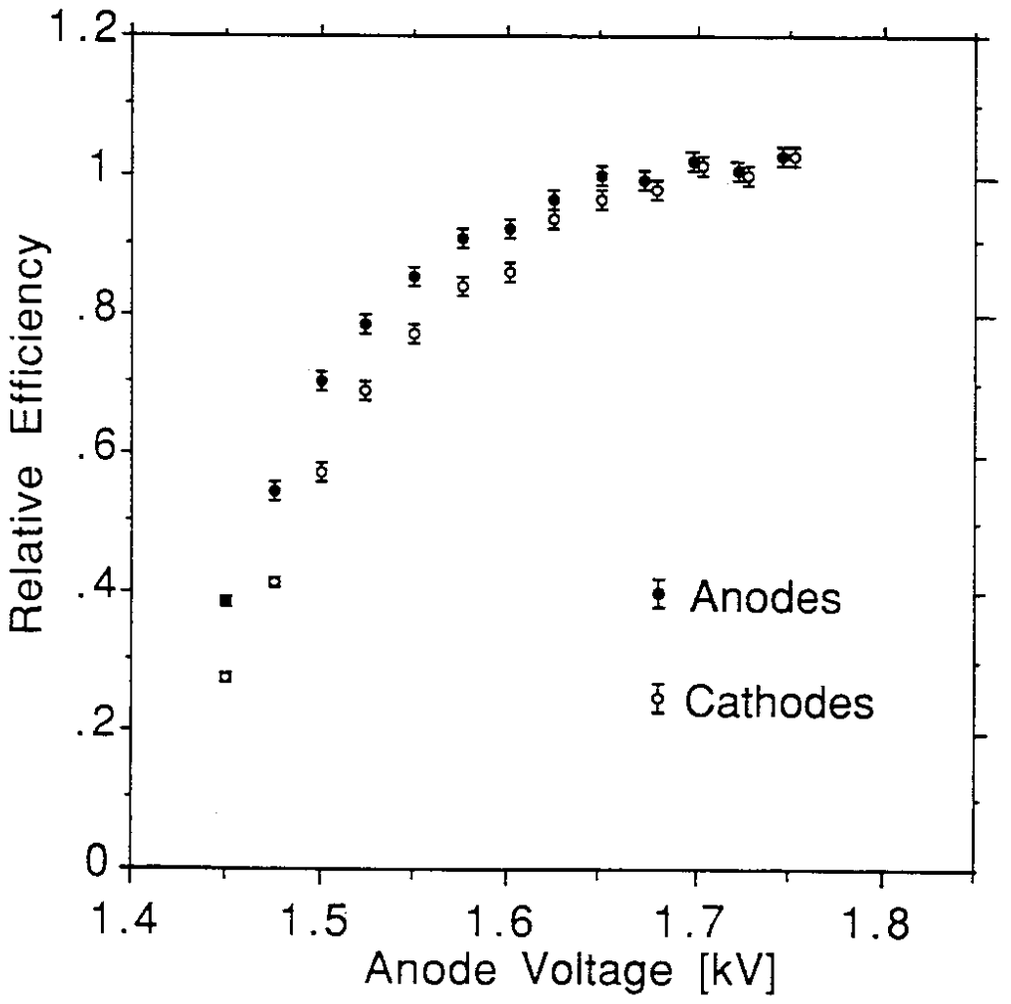

Figure 10: Plateau curves of anode and cathode counting rates measured with single photo-electrons.

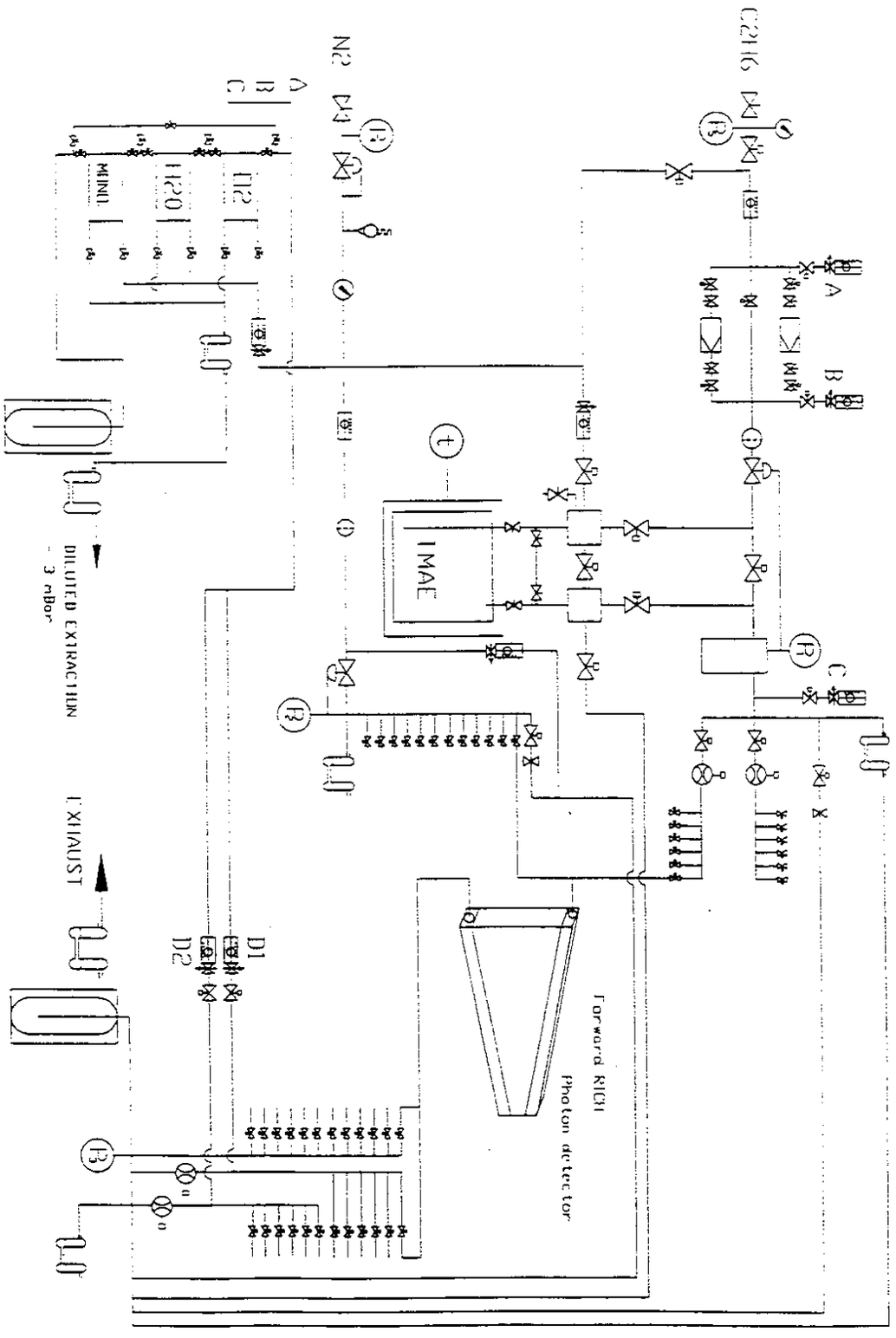

Figure 11: The driftgas flow diagram.

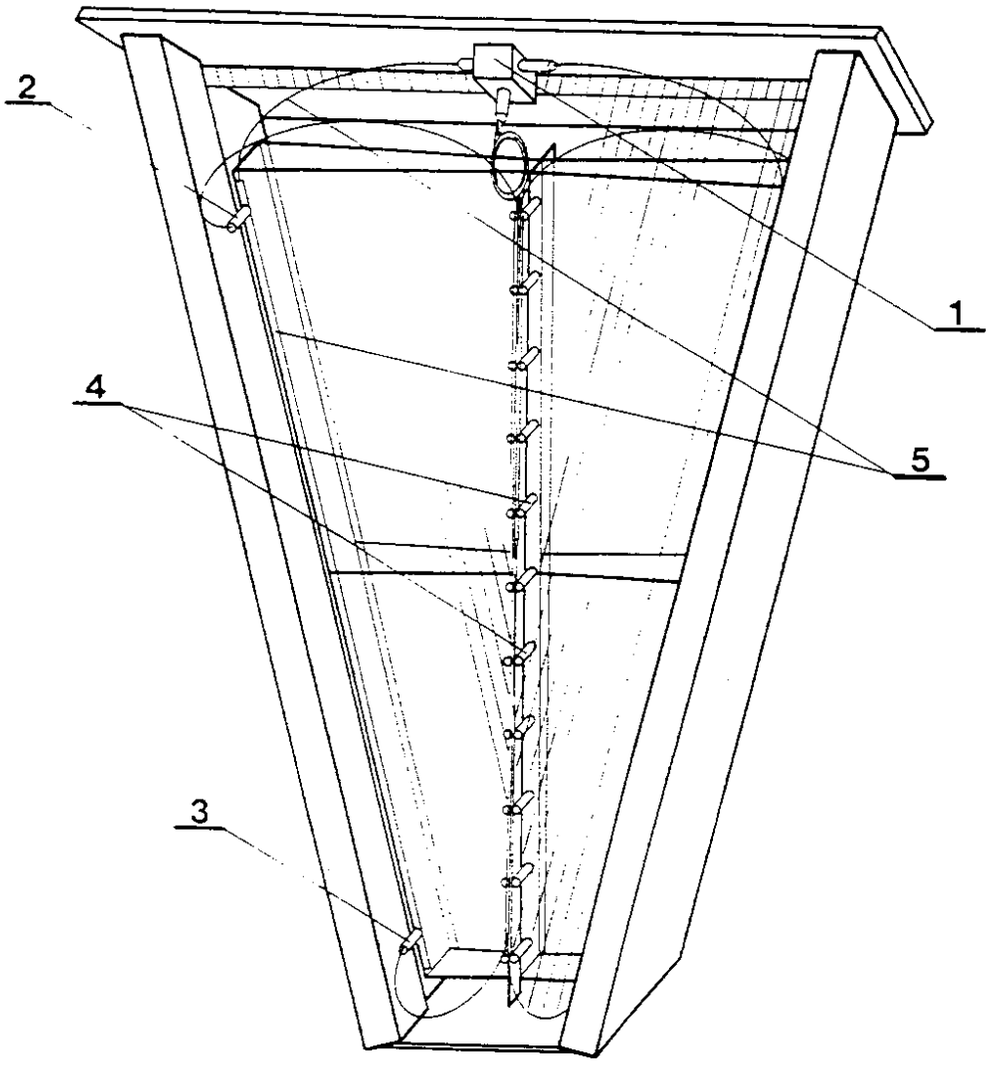

Figure 12: The calibration system of the Forward RICH detector: 1 = Hydrogen flash lamp; 2 and 3 = alignment fibres; 4 = calibration fibres (22 light spots); 5 = engraved quartz rod.

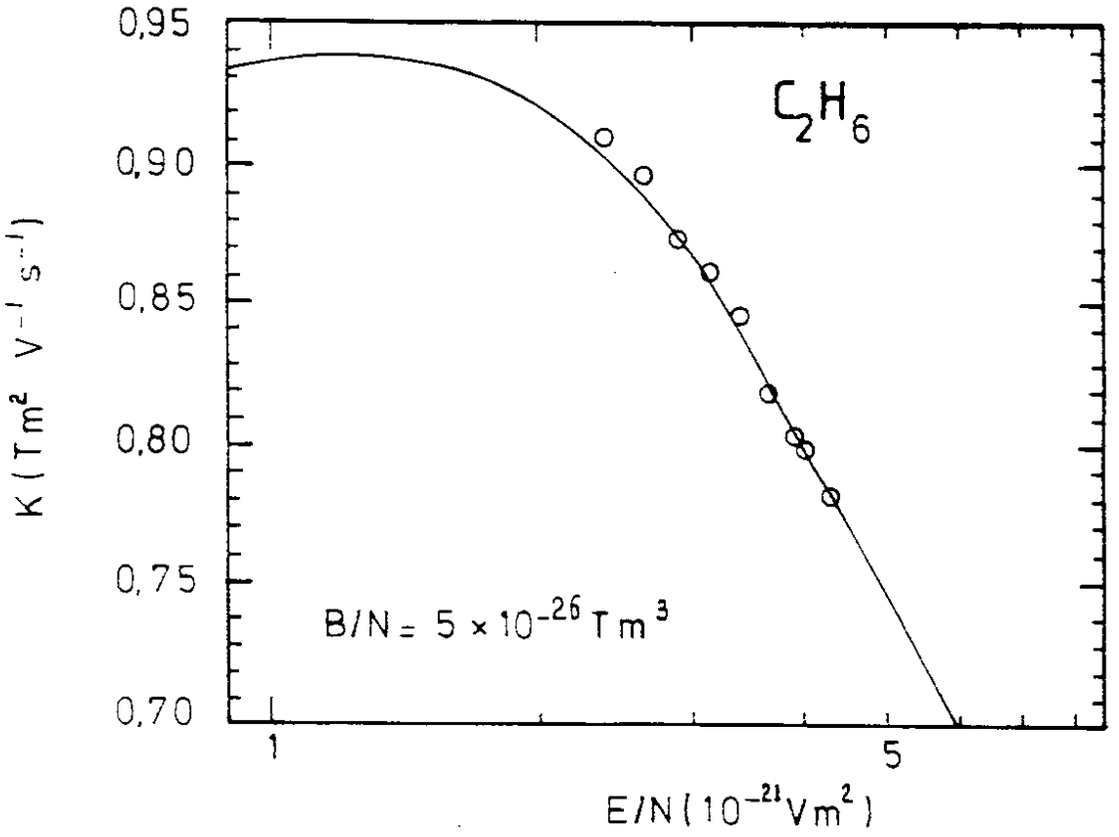

Figure 13: The quantity k = v_dB/($E_d \sin\theta_L$) versus the reduced drift field in ethane in the presence of a reduced magnetic field B/N = 5 × 10^{-26} T m^3. The dots represent measured values, the curve shows the calculation by [13].

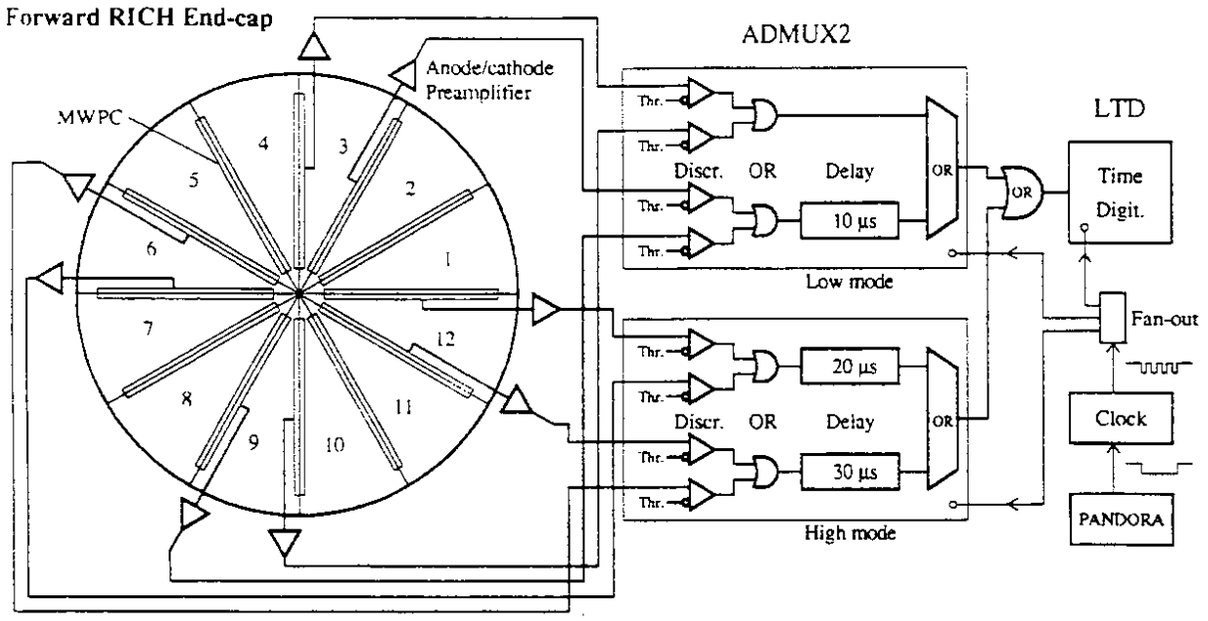

Figure 14: Elements of the electronics chain.

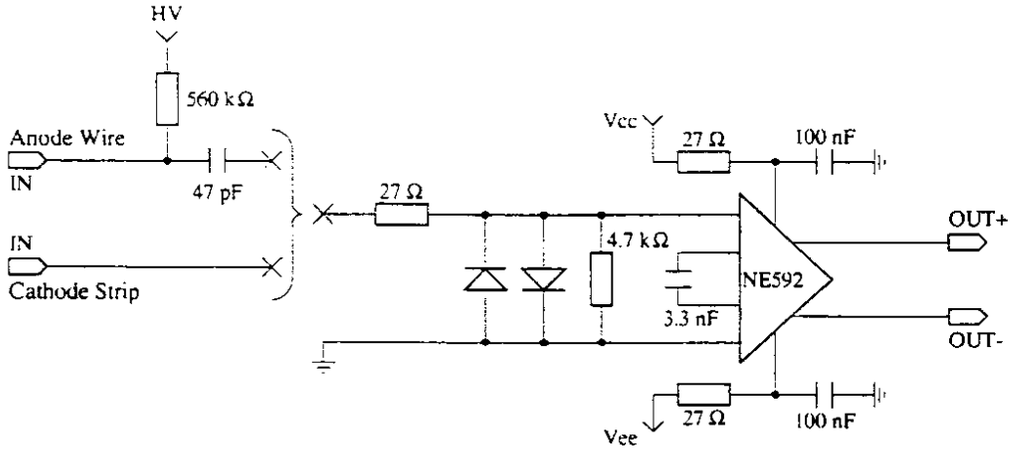

Figure 15: Circuit diagram of the present preamplifier.

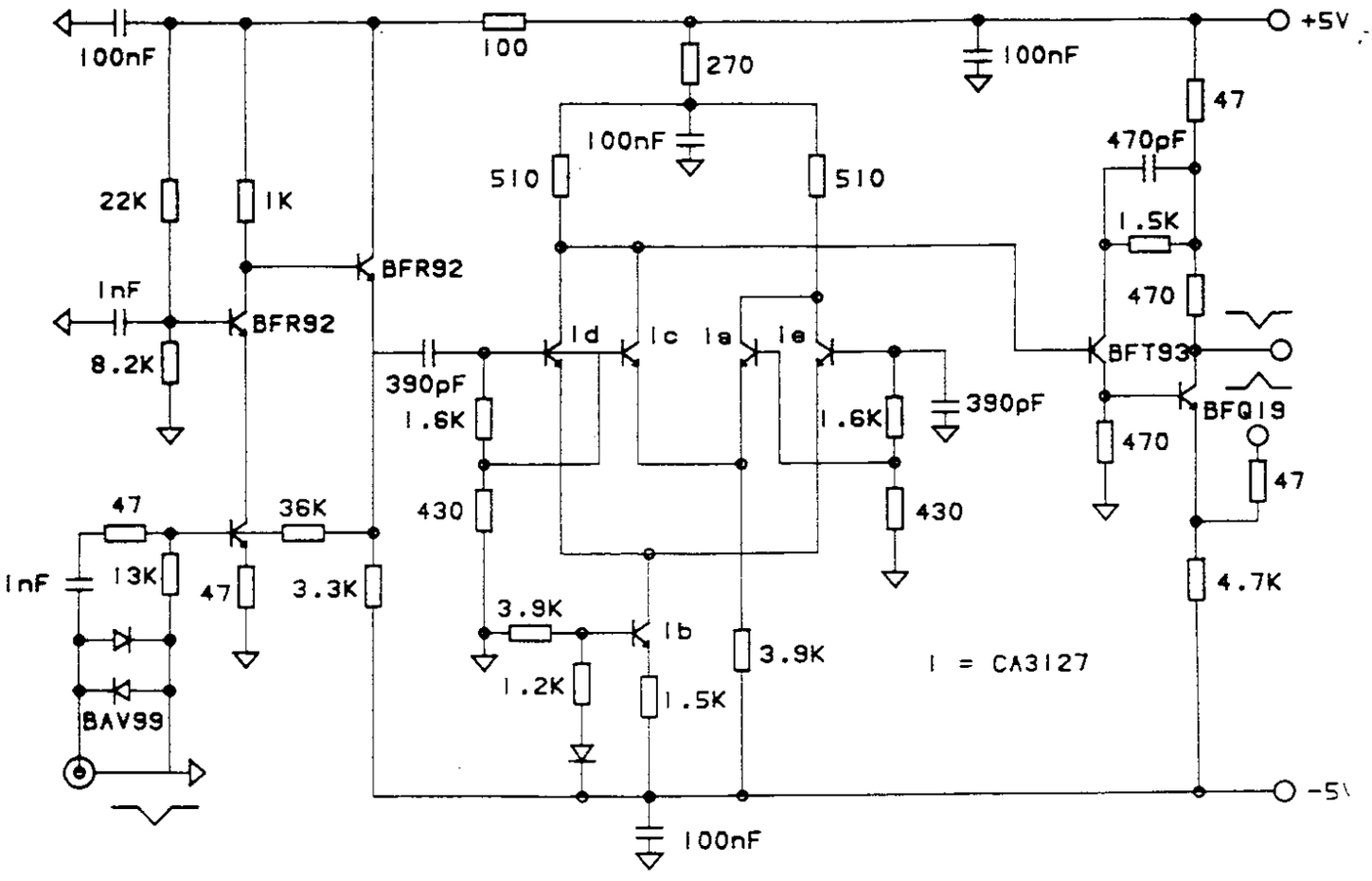

Figure 16: Circuit diagram of the anode version of the logarithmic preamplifier.

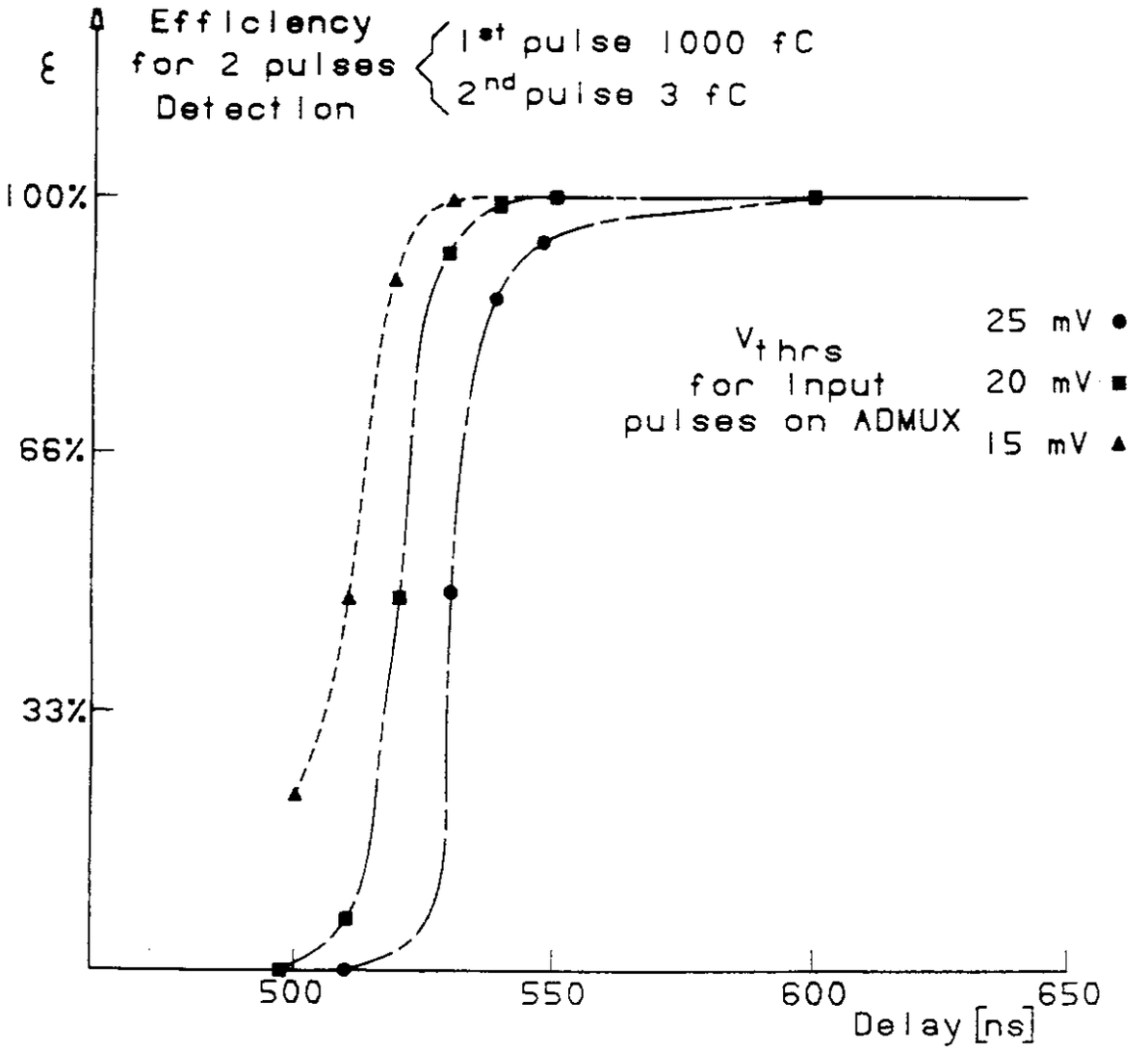

Figure 17: Pulse separation with the logarithmic preamplifier. The efficiency for detecting a 3 fC pulse injected after a 1000 fC pulse is plotted against the time separation between the two pulses, for different discrimination thresholds.

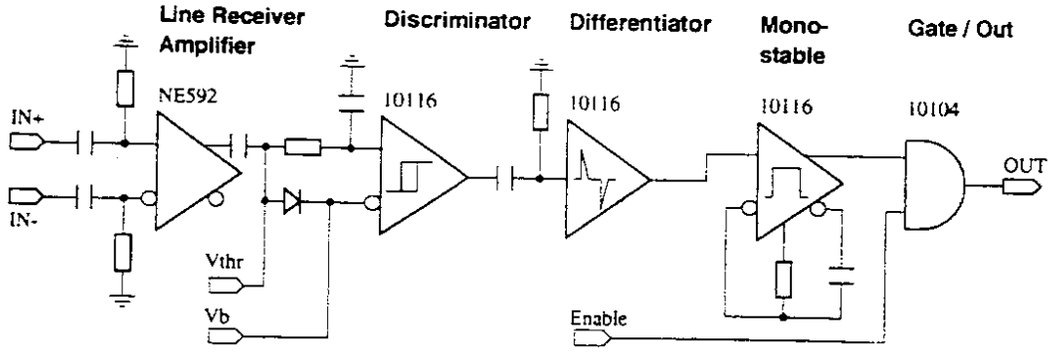

Figure 18: Discriminator circuit diagram.

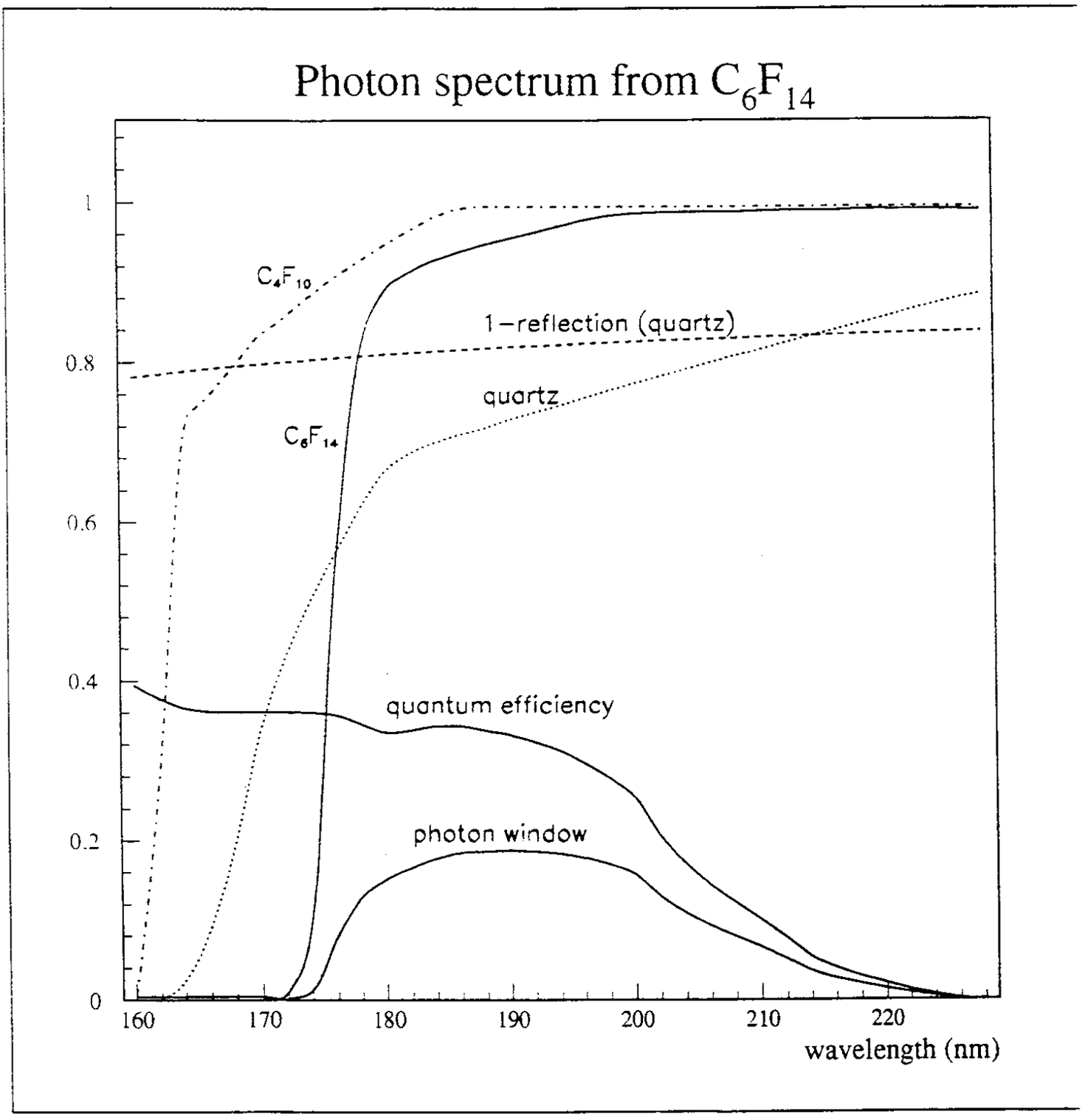

Figure 19: The photon spectrum from the C_6F_{14} liquid radiator.

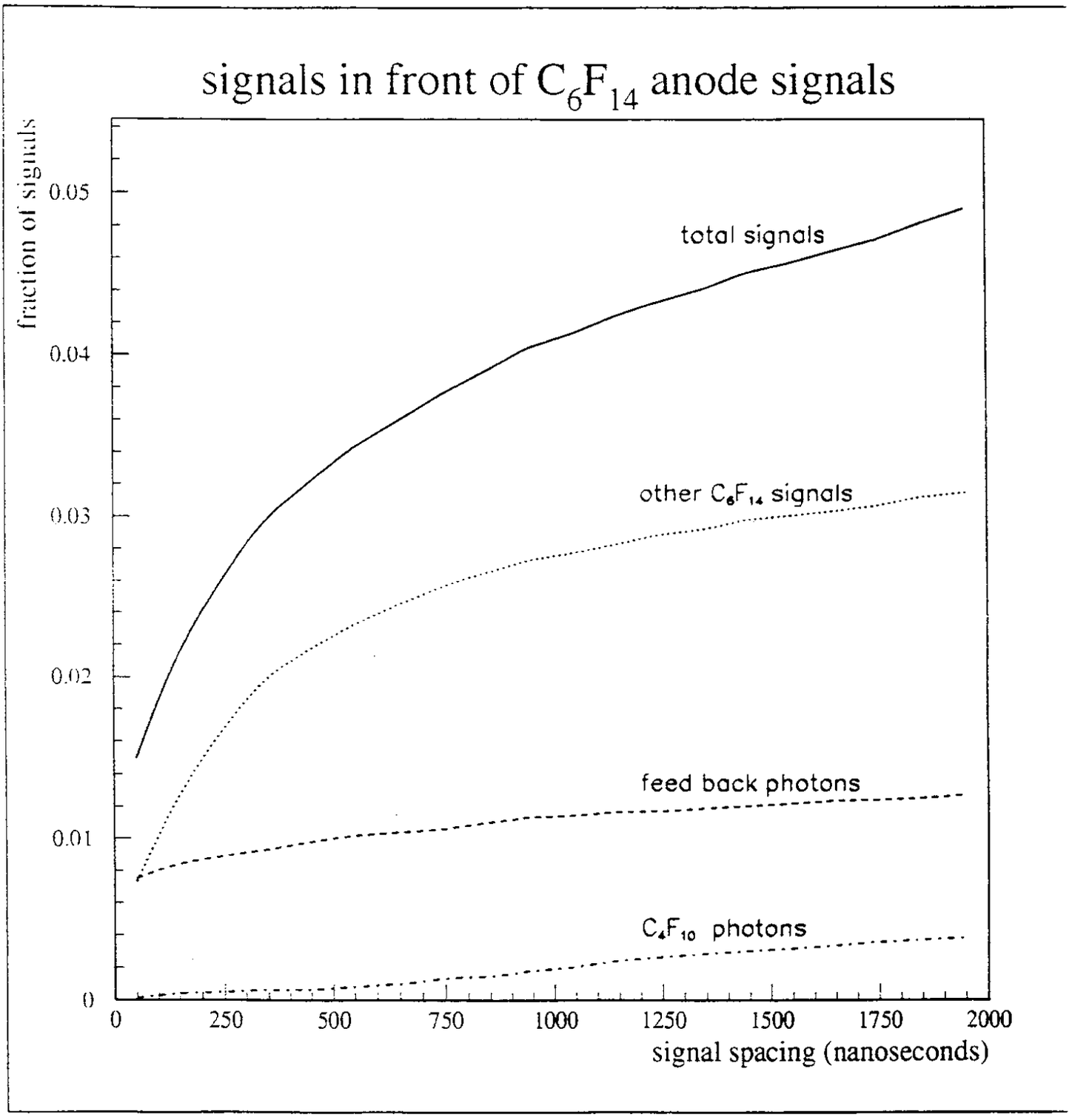

Figure 20: Signals arriving before C_6F_{14} anode signals.

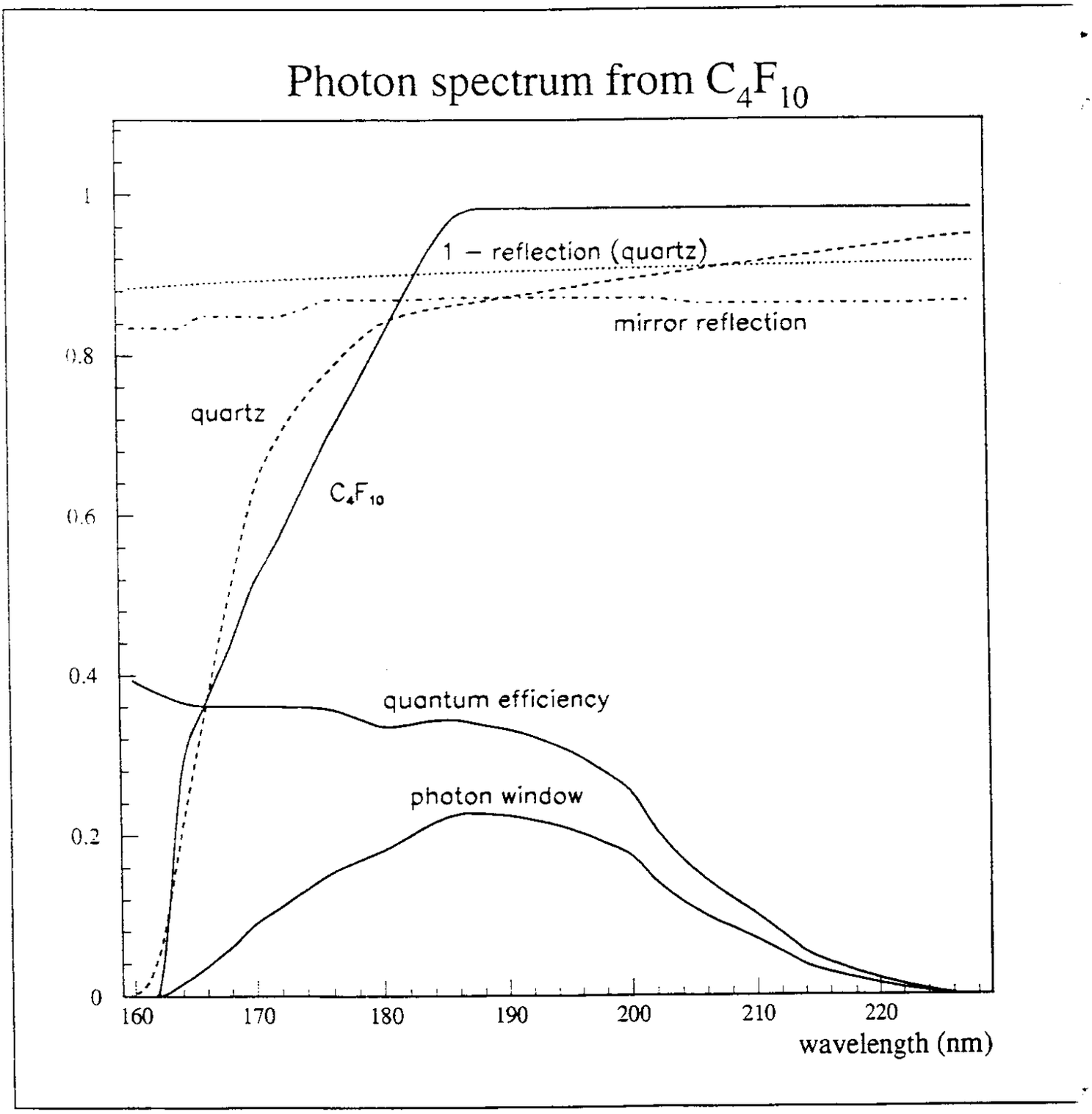

Figure 21: Photon spectrum from the C_4F_{10} gas radiator.

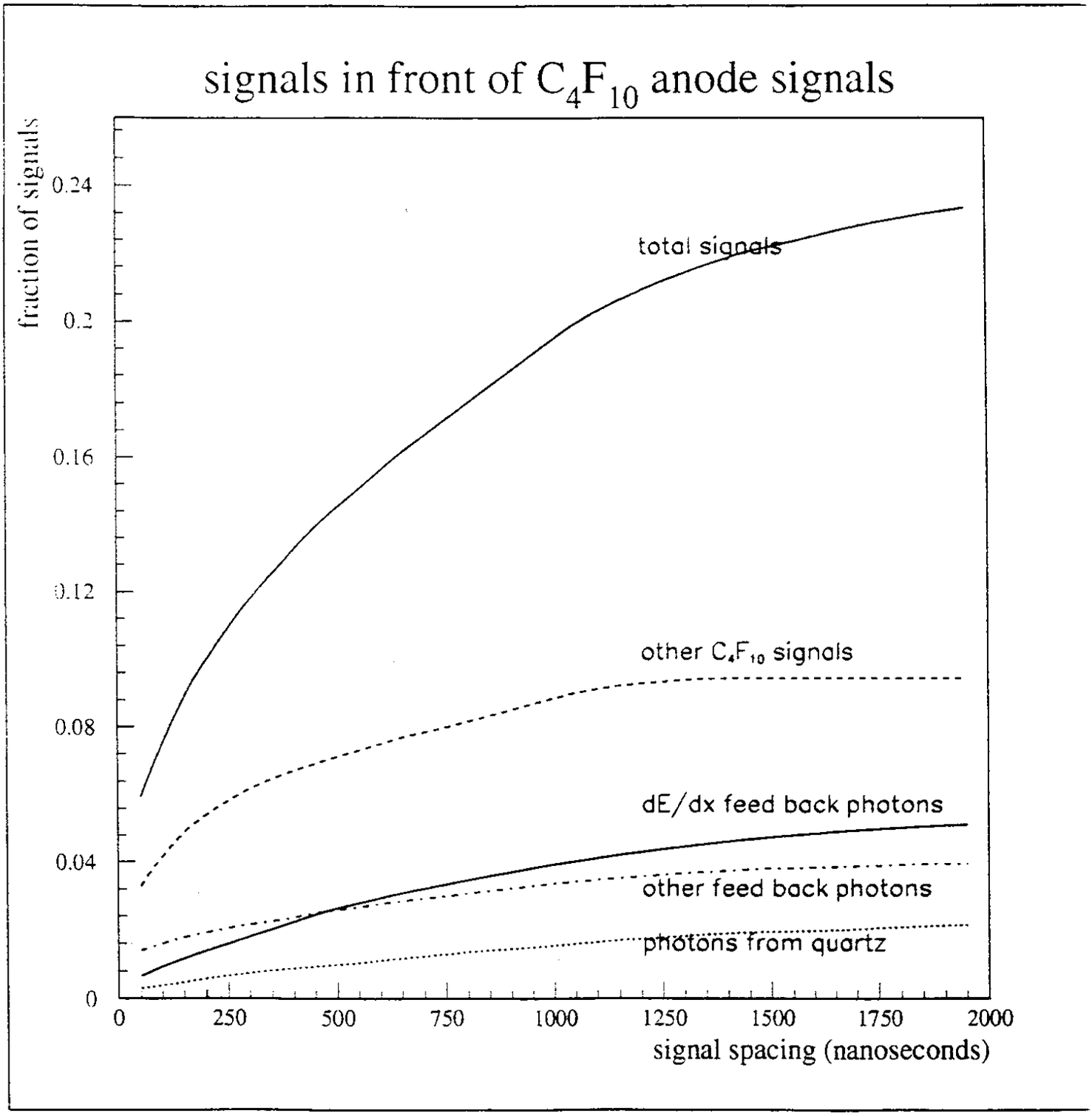

Figure 22: Signals arriving before C_4F_{10} anode signals.

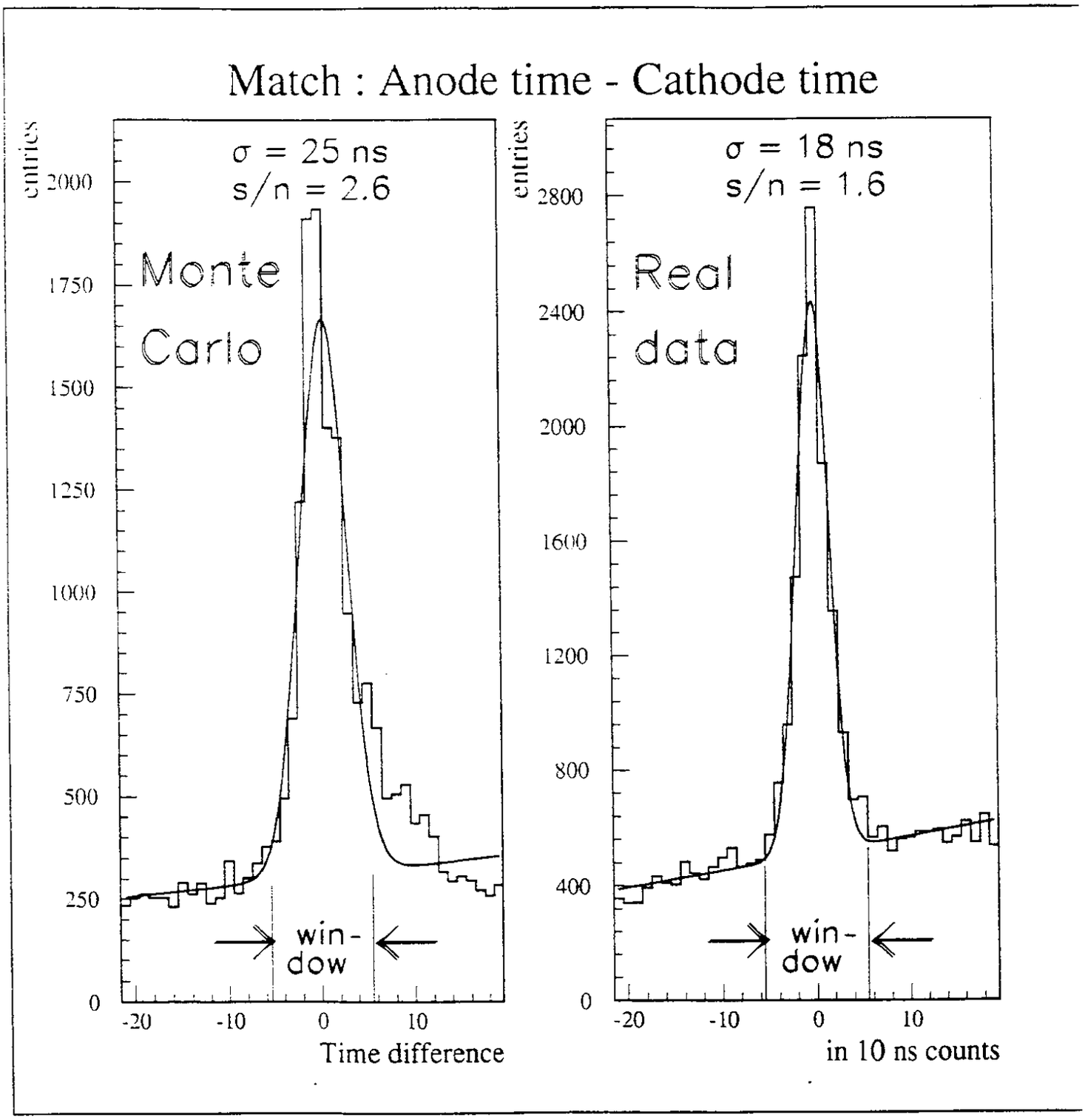

Figure 23: Time difference between corresponding anode and cathode signals in real data and in simulation.

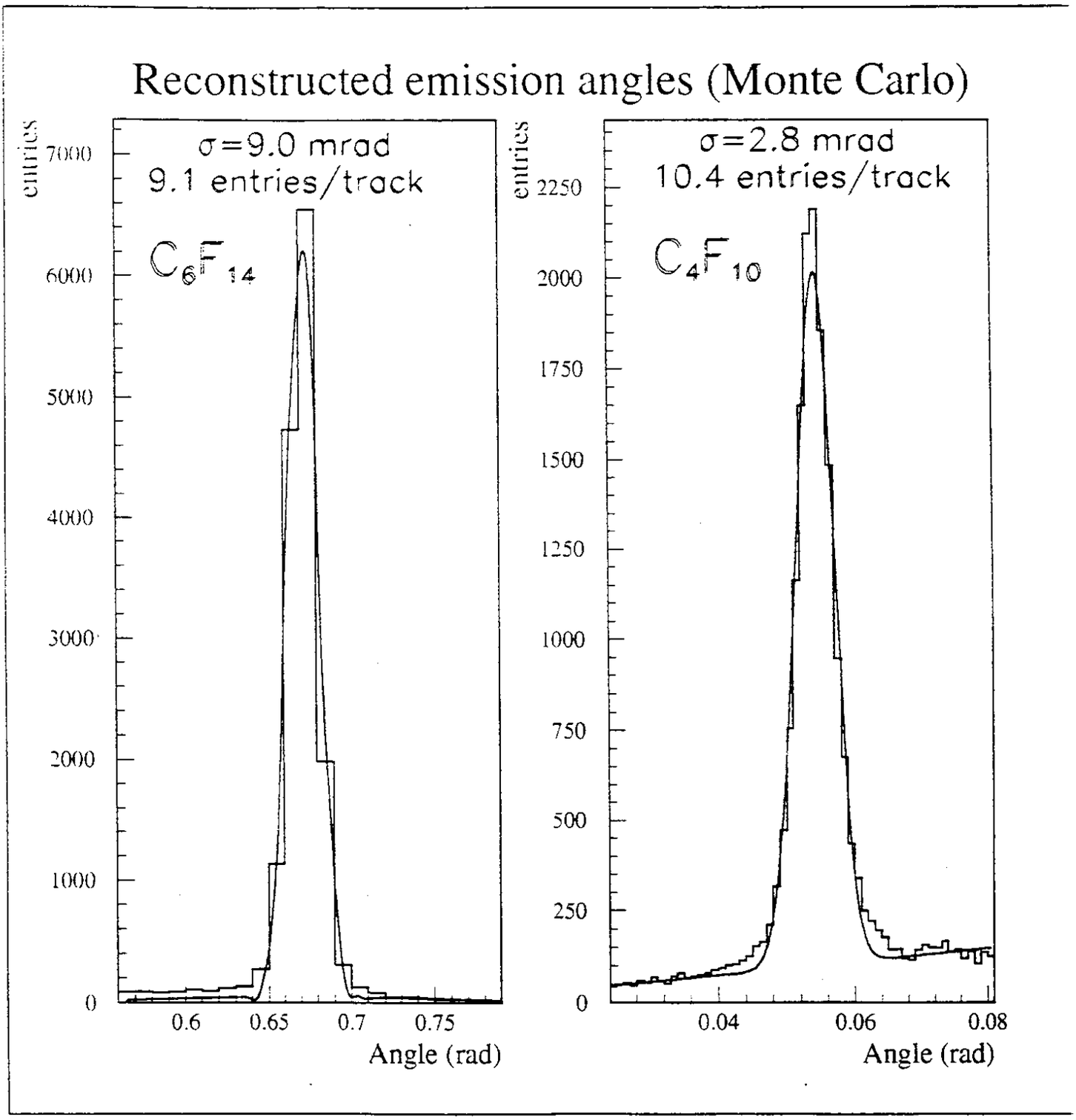

Figure 24: Cherenkov angles from C_6F_{14} and C_4F_{10} photons according to simulation.

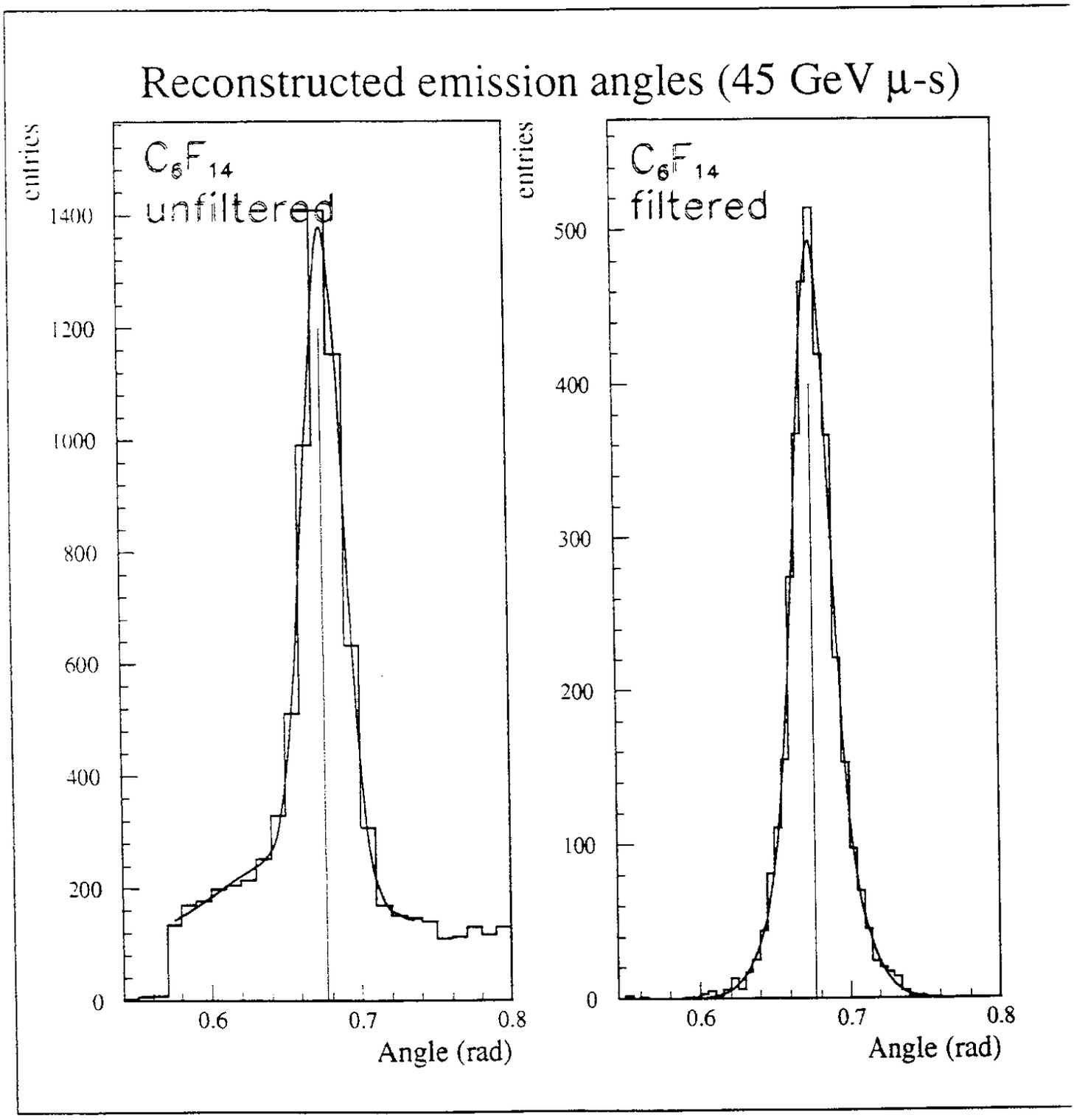

Figure 25: Observed distribution in Cherenkov angle for C_6F_{14} photons from 45 GeV/c muons, before and after application of a noise filter.

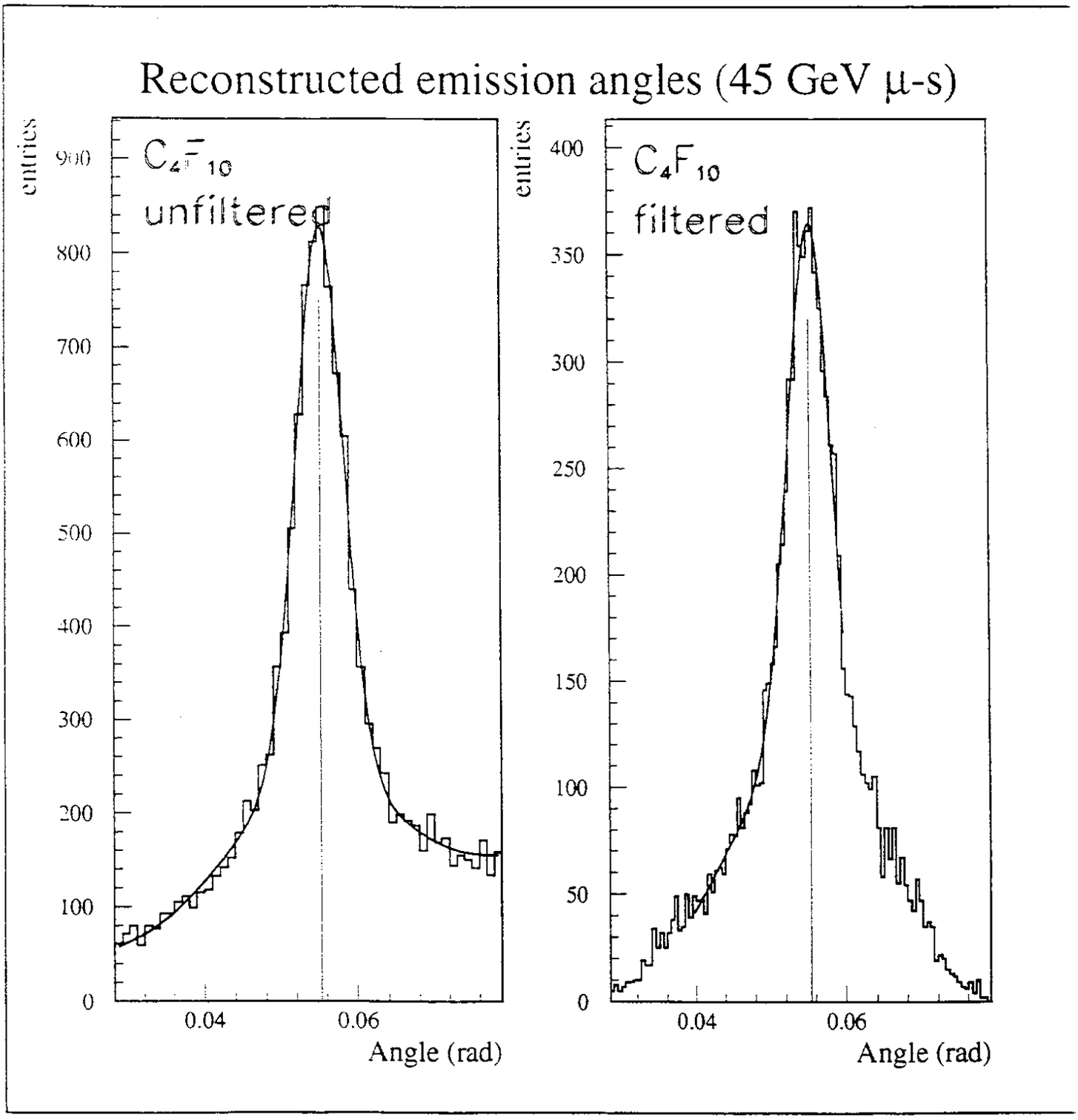

Figure 26: Observed Cherenkov angles for C_4F_{10} photons from 45 GeV/c muons.

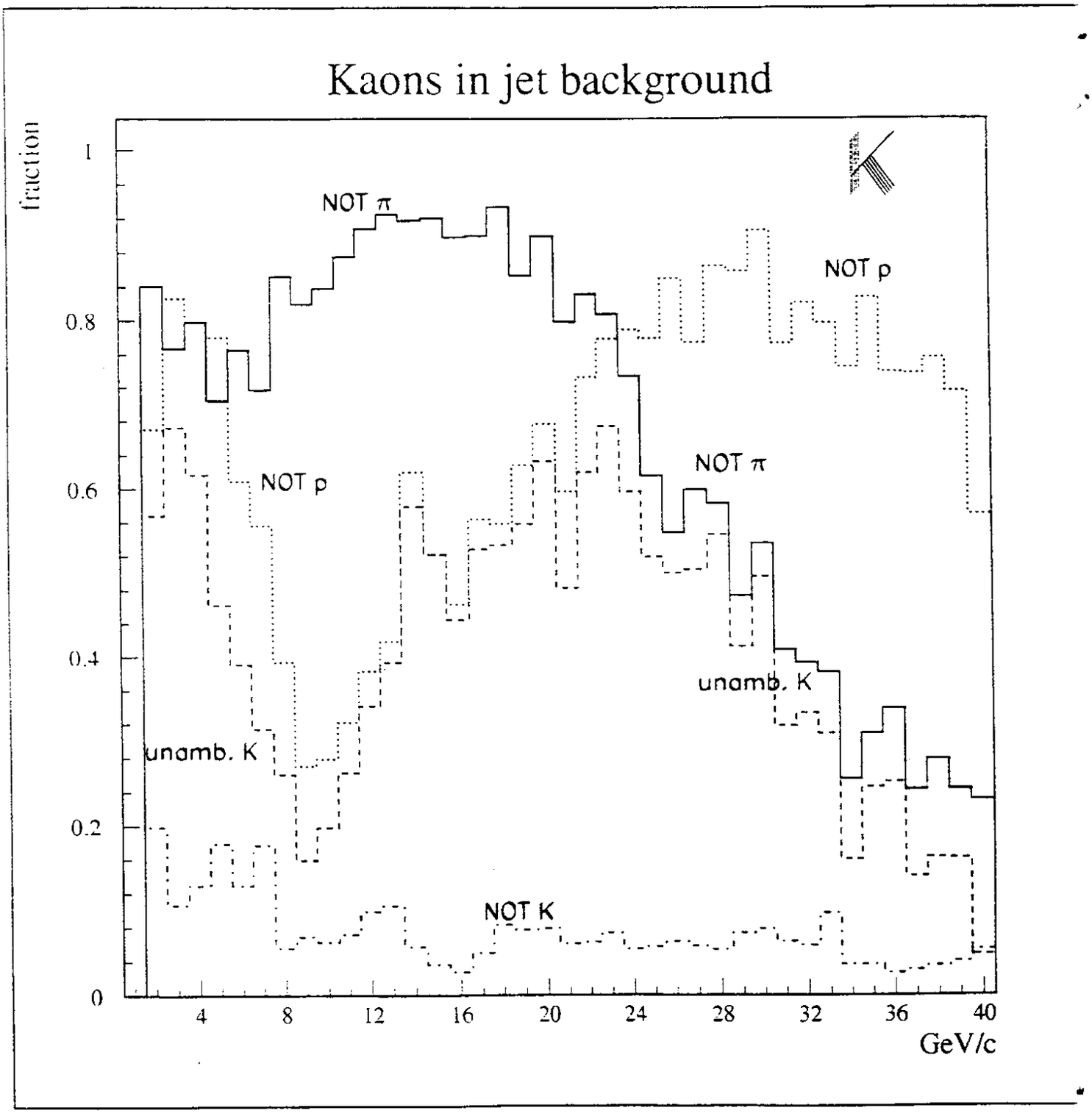

Figure 27: Identification of simulated kaons superimposed on a jet background as a function of momentum (from [21]).

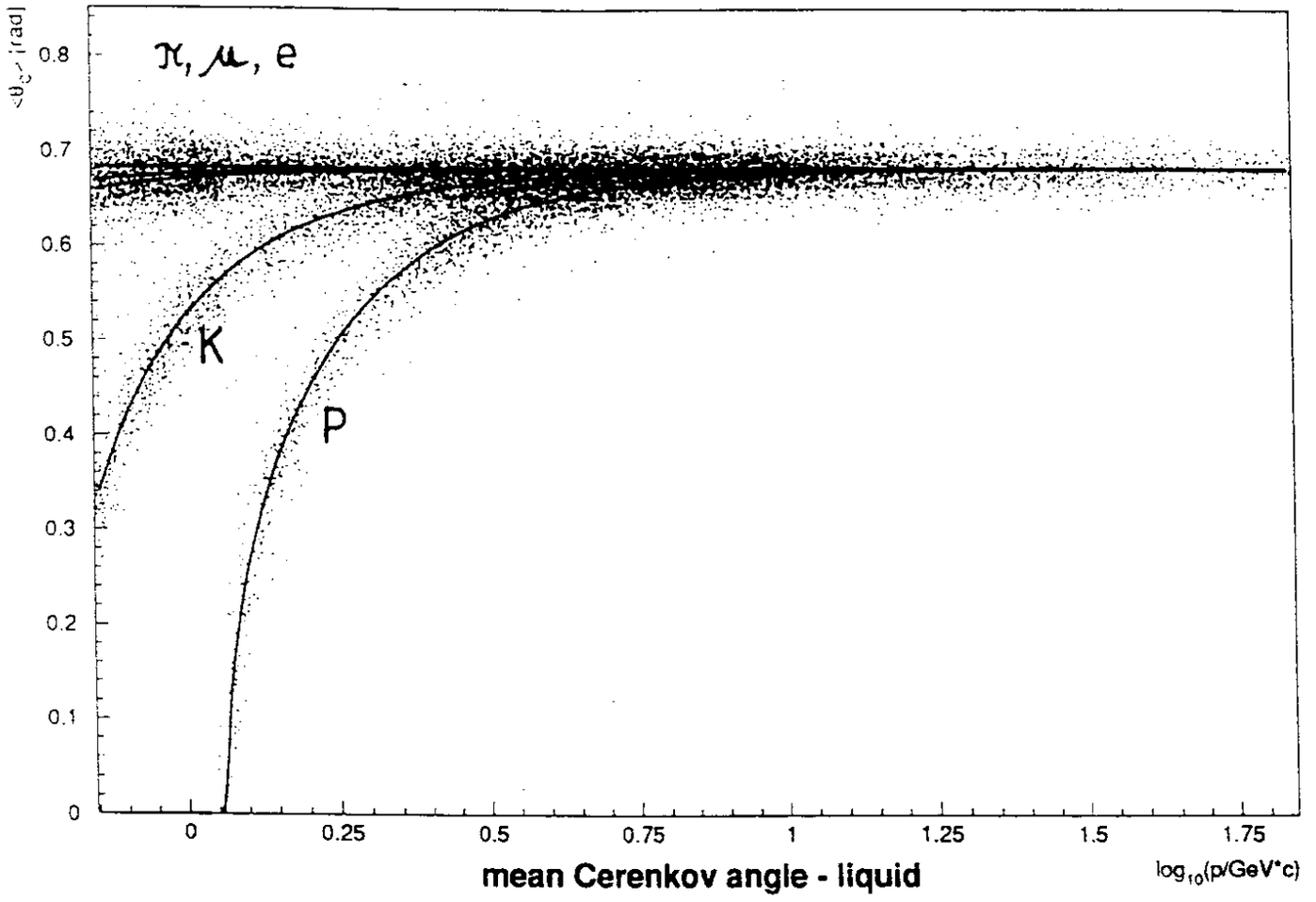

Figure 28: Liquid radiator data: mean Cherenkov angle as a function of particle momentum. The angles shown are the unambiguous result of a set of robustified least squares estimates. The fits used photons in a 5σ band around each mass hypothesis.